INVITED PAPER: FUNCTIONAL COATINGS, THIN FILMS AND MEMBRANES (INCLUDING DEPOSITION TECHNIQUES)

CrossMark

Inkjet printing of functional oxide nanostructures from solution-based inks

Aleksander Matavž [1,2] · Barbara Malič [1,2]

Abstract

The inkjet printing of functional oxide nanostructures from solutions provides many advantages when compared to conventionally used top-down patterning methods. It does not require masks and—as the material is deposited only where and when needed—any material-removal steps are not needed. This contributes to reduced waste, cost, and time required to fabricate the device. Despite its apparent simplicity, the inkjet printing process offers many challenges, including the ink chemistry, ink-substrate interaction, and drying; these are discussed in the present review. The ink should have suitable values of viscosity, surface tension, density, and vapor pressure to fulfil the requirements for stable drop formation and pattern formation. The substrate properties are discussed from the points of view of wetting and stability of the printed patterns. Drying of wet deposits without build-up of the material at the edges via the coffee-stain effect is a critical step and strategies to overcome it are discussed. Finally, the potential of inkjet printing technology in many different applications is discussed.

Graphical Abstract

In the inkjet printing of functional oxide nanostructures from solutions the material is deposited only where and when needed which contributes to reduced waste, cost and time required to fabricate the device. Despite its apparent simplicity, the inkjet printing process offers many challenges, including the ink chemistry, ink-substrate interaction, and drying; these are discussed in the review.
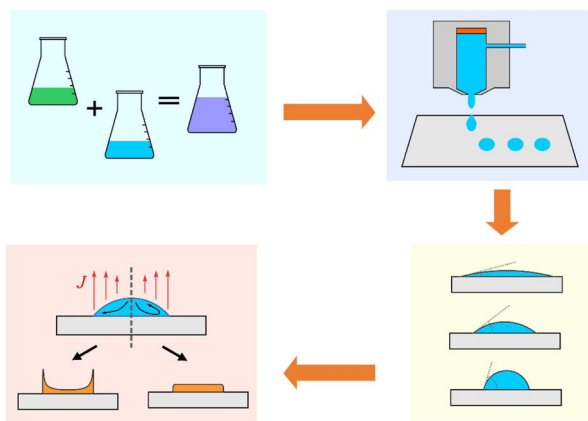
✉ Barbara Malič
barbara.malic@ijs.si

1   Jožef Stefan Institute, Jamova cesta 39, Ljubljana SI-1000, Slovenia

2   Jožef Stefan International Postgraduate School, Jamova cesta 39, Ljubljana SI-1000, Slovenia

⚛ Springer

Highlights

- Inkjet printing enables integration of different materials into components without additional steps.
- Functional oxide nanostructures are patterned from solution-based inks.
- Control over wetting and drying is achieved through understanding ink-substrate interaction.

Keywords Direct writing · Printed electronics · Sol–gel · Substrate · Wetting · Coffee-stain effect

1 Introduction

Inkjet printing has been in use for more than half a century to print documents in small offices and homes. More recently, it has been recognized as a highly flexible manufacturing tool in 2D and 3D applications. Easy pattern modifications, micrometer resolution, and the absence of additional patterning steps make inkjet printing attractive for the manufacture of electronic devices. This has governed the development of printed electronics—a huge market based on the production of low-cost, large-area electronics.

The printing process relies on the accurate generation of small droplets of a liquid, which are ejected from a reservoir through a nozzle and deposited at digitally determined locations on a substrate. There are two modes of drop formation: continuous and drop-on-demand (DOD) [1]. Due to better accuracy, smaller drop size, and larger flexibility, DOD printing is better suited for home/small office and research applications. In order to form the droplets only when needed, the fluid is modulated by an acoustic wave that is generated by thermal or piezoelectric excitation. Thermal DOD is typically used for conventional printing applications, while for the patterning of functional materials in research piezoelectric DOD inkjet printing prevails. DOD inkjet printing is the topic of this review.

In piezoelectric inkjet printing an electric signal, often referred to as a waveform, is applied to a transducer (Fig. 1). The design of the waveform determines the jetting stability, the drop size, and its velocity. The simplest waveform consists of a trapezoid with a positive voltage (the left-hand part of the waveform shown in Fig. 1b); however, additional segments are often added. A pulse of the opposite voltage can follow the initial pulse, with the objective being to cancel out the remaining oscillations present in the print-head (waveform shown in Fig. 1b) [2]. After successful ejection from the nozzle, the drop lands at a predetermined location on the substrate. The substrate and the print-head move during the printing process to determine the location of the deposited material. In theory the process is simple; however, in practice it can become challenging. The specific requirements of the fluid represent a major restriction for inkjet printing. The ink should have a viscosity and a surface tension that are within certain ranges, roughly 10–12 mPa s and 28–33 mN m^{-1}[3]. A Newtonian behavior of the viscosity is preferred, because viscoelastic effects could cause problems with the jet breaking up into drops. The wrong ink design can result in the formation of satellite drops, dripping through the print-head nozzles, orifice plate wetting, and nozzle clogging [4, 5].

A large number of parameters—spanning from specific fluid requirements to drying—contribute to the complexity of the inkjet printing process. General guidelines have been established in terms of stable drop formation [6], the stability of the printed lines [7, 8], and the uniformity of the dried deposits [9, 10]. Depending on the physical form of the solute in the ink we distinguish solution-based inks, where the solute is completely dissolved in a particular solvent, and particle-dispersion based inks, where the solid (nano)particles are dispersed in a liquid medium. In this review we only discuss solution-based inks, which are used
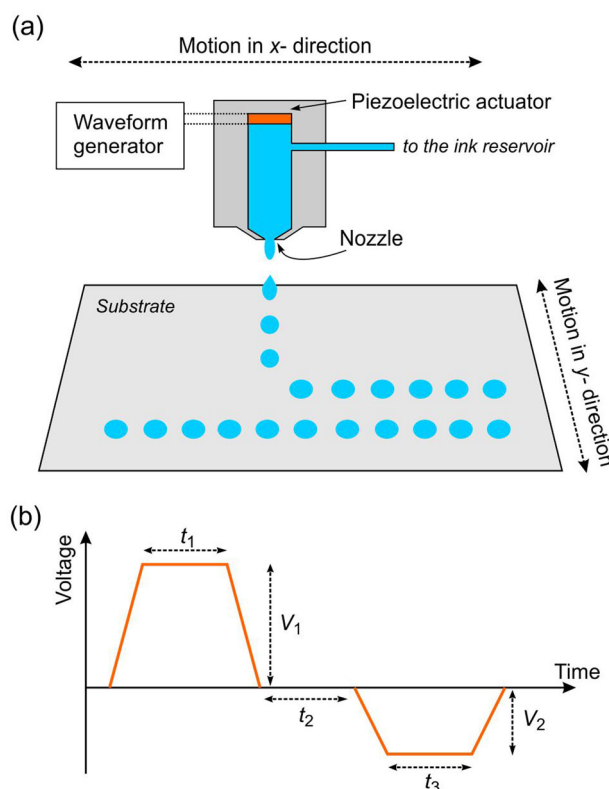
Fig. 1 **a** Schematic representation of piezoelectric drop-on-demand inkjet printing. **b** A typical waveform that is applied to a piezoelectric actuator for the ejection of a drop

Fig. 2 Schematic representation of the inkjet printing process. Symbols correspond to: $\theta_{A,R}$ advancing and receding contact angles, p - drop spacing, v_T transverse print-head velocity, T temperature, $p_{i,j}^{sat}$ saturated vapor pressure, $\gamma i,j$ surface tension, $D_{i,j}$ diffusion coefficient, η viscosity, t time, d layer thickness
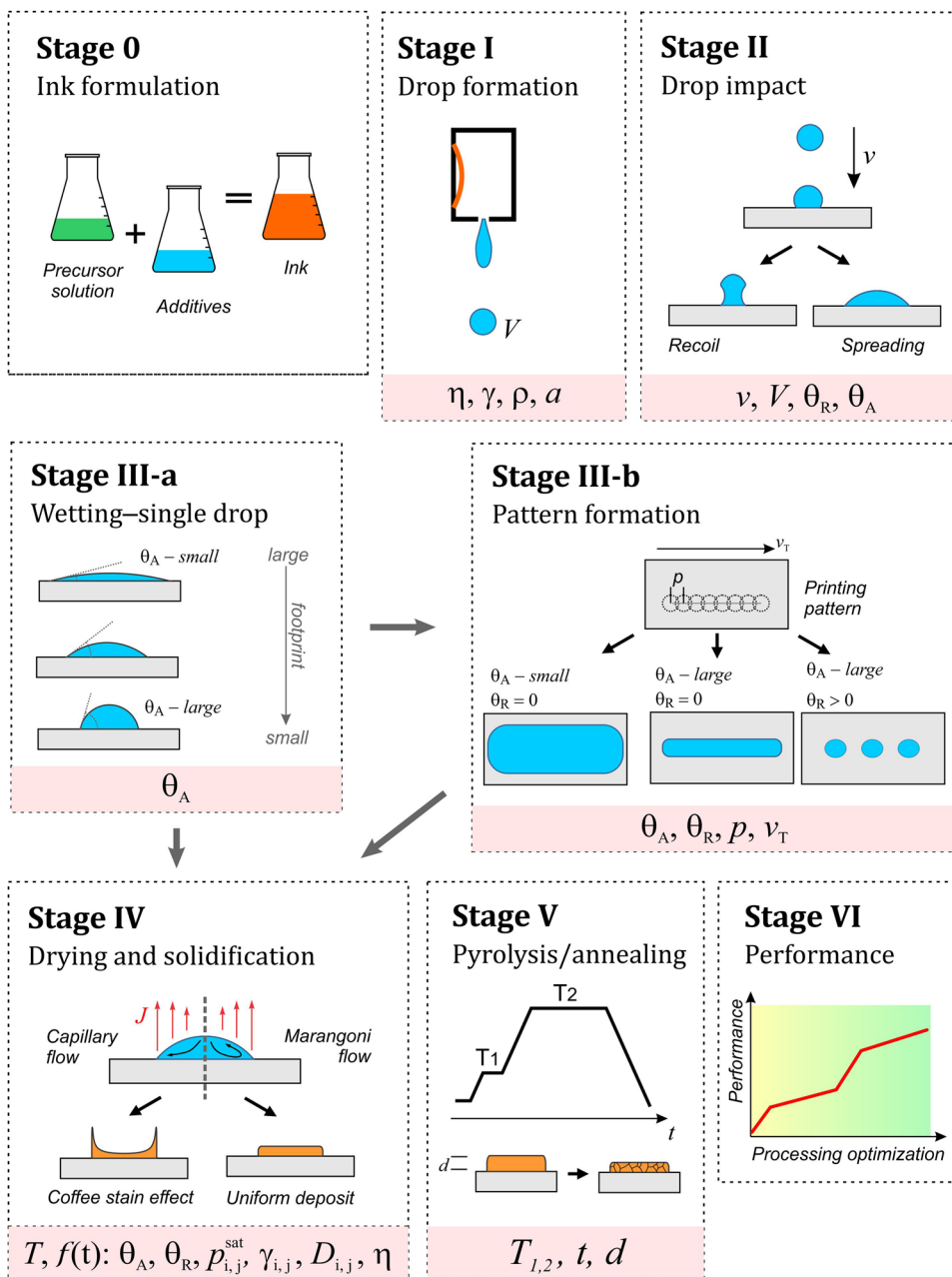
to pattern layers with thicknesses from a few nanometers to roughly the micron range.

The inkjet printing process is schematically shown in Fig. 2. The pre-printing phase (Stage 0) is the formulation of the ink, keeping in mind that the operating principles set certain limits on the ink's physical properties. The viscosity (η), surface tension (γ), and density (ρ) need to be balanced for a stable drop formation, and the vapor pressure should be low enough to prevent clogging of the nozzle(s). After successful ejection (Stage I), the drop eventually collides with the substrate (Stage II) and undergoes several shape changes until it reaches an equilibrium state. In the latter,

the drop wets the substrate according to the balance of the surface energies of the ink and the substrate. The wetting (Stage III-a) is quantified by the contact angle. With a decreasing contact angle the diameter of the printed drop increases; the wetting thus strongly impacts on the resolution. Depending on the printing pattern, individual drops can overlap to form more complex geometrical objects, such as lines and rectangles (Stage III-b). In this case the wetting directly affects the shape of the pattern: a low contact angle results in large and poorly defined patterns, while a high contact angle promotes the occurrence of pattern instabilities. After the printing process the wet

pattern is dried, which transforms it into a solid deposit (Stage IV). Drying often produces a pattern with pronounced edges, which is known as the "coffee-stain" effect [11]. Several factors influence the morphology of a dried deposit, including the solvent's formulation, the substrate's surface properties, the humidity of the air and the temperature. Finally, the dried deposit is heated to decompose the organic residues in the so-called pyrolysis step, and obtain the functional metal oxide. Depending on the material and the application, the heating conditions are selected to result in amorphous or crystalline material with a certain microstructure (Stage V). Process optimization usually contributes to better performance of the functional oxide (Stage VI).

This review article addresses the individual stages of the inkjet printing process—starting with the ink's formulation and concluding with applications. We devote special attention to the ink's formulation, wetting and drying, which were not comprehensively covered by earlier reviews [12–16].

2 Ink formulation

2.1 Drop formation

The ink's formulation should fulfill the fluid requirements, depending on the specific printer type. The flow of the ink through the nozzle is described by fluidic mechanics, or more specifically by the dimensionless Reynolds (Re) and Weber (We) numbers, Eqs. 1 and 2. The Ohnesorge number (Oh), which is the ratio $\sqrt{We}/Re$ (Eq. 3), includes all the fluid's physical properties relevant to the drop's formation, i.e., the viscosity, η, the surface tension, γ, and the density, ρ [17].

$$Re = \frac{v\rho a}{\eta} \tag{1}$$

$$We = \frac{v^2 \rho a}{\gamma} \tag{2}$$

$$Oh = \frac{\eta}{\sqrt{\rho \gamma a}} \tag{3}$$

where v is the fluid velocity and a is a characteristic dimension, in our case the diameter of the nozzle.

In the literature, the inverse of the Ohnesorge number—also known as the Z number—has often been used in relation to the drop formation. Reis and Derby [6] used numerical modeling to investigate the drop formation in inkjet printing and proposed the range $1 < Z < 10$ for stable drop formation. The experiments show that the Z range for stable drop formation depends on the ink formulation and the waveform used [12, 18, 19]. For example, Jang et al. [20] showed for ethylene-glycol–water mixtures that Z values between 4 and 14 produce stable drops.
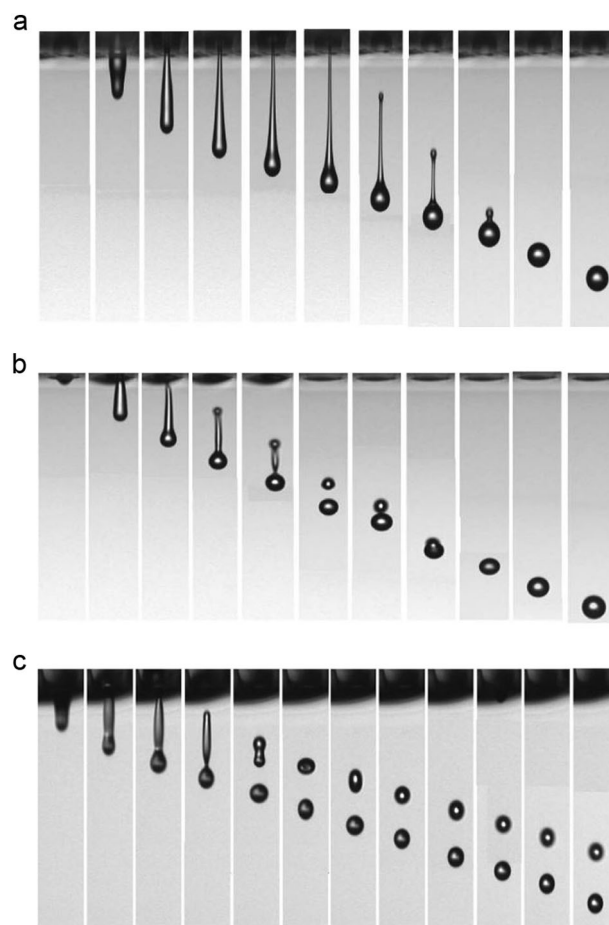

Fig. 3 Sequence of stroboscopic images showing the drop formation during the inkjet printing of ethylene-glycol–water mixtures with different Z values: **a** $Z = 2.2$, **b** $Z = 6.6$, **c** $Z = 17.3$. The drops were jetted at a constant driving voltage of 25 V and a frequency of 1 kHz. The photographs were taken using a stroboscopic camera with 20-μs decay. Reproduced with permission from [20]. Copyright 2009, American Chemical Society

The stable drop formation is limited by two extremes, i.e., the low and high Z numbers. At low Z values, the high viscosity inhibits the drop's ejection, i.e., the pressure required for the drop's ejection is too large. By increasing the Z value to the lower limit of the printable range, the ejected drops have long tails (Fig. 3a, $Z = 2.1$). For $Z = 6.6$, the tail of an ejected drop first separates from the main drop and forms a satellite drop, which later merges with the main drop (Fig. 3b). At even higher Z values, the ejected drop separates into two or more satellite drops (Fig. 3c, $Z = 17.3$), which remain separated from the main drop. The occurrence of satellite drops should be avoided as they reduce the resolution of the printing.

2.2 Chemical solution deposition (CSD)

A common approach to formulating a solution-based ink is to first synthesize a functional oxide precursor solution for

the CSD of thin films, and then adjust its physical properties to reach the values suitable for inkjet printing, see ref. [21–23].

The CSD of functional oxide thin films has been the subject of many reviews and books, for example ref. [24–26], and only a brief overview of CSD is given here. Depending on the solution chemistry, we distinguish the sol–gel, chelate or hybrid routes. The synthesis of a precursor solution (also called a sol) involves the dissolution of one or more metal reagents in a suitable solvent or a mixture of solvents, usually followed by a reaction.

Metal reagents include metal alkoxides, $M(OR)_n$ [27], and/or short-chain or long-chain carboxylates, $M(R\text{-}COO)_n$ [28], or both, either mixed or undergoing a reaction [29]. Metal nitrates, $M(NO_3)_n$, have also been used due to their good solubility in organic solvents [30, 31]. The reactivity of transition-metal alkoxides is often reduced by the addition of small amounts of alkanolamines, e.g., $NH_2\text{-}(CH_2)_n\text{-}OH$, or $HO\text{-}(CH_2)_n\text{-}NH\text{-}CH_2)_{n'}\text{-}OH$, β-diketones, $R_1\text{-}CO\text{-}CH_2\text{-}CO\text{-}R_2$, or carboxylic acids, $R\text{-}COOH$. The choice of solvent is dictated by the choice of the reagents, which need to be fully dissolved, and the solution should be stable for weeks or even months. The concentrations of the solutions are quite low, usually in the range of a few 0.01 M to a few 0.1 M. Frequently used solvents include alkyl alcohols and ether alcohols, some of which are collected in Table 1. The common features of these solvents include low viscosity and low surface energy, implying good wettability and spreading on a substrate, and low boiling points to enable easy solvent removal upon drying. We note that diols, such as the 1,3-propanediol (PD) used in the diol-based route, are not included in this list [32].

In CSD the sol is deposited on a suitable substrate, very often by spin-coating [33]. In the drying and pyrolysis steps the evaporation of residual solvent(s), continued reactions, dehydroxylation, thermal oxidation of functional groups and usually partial densification occur. The crystallization step is needed to establish the long-range order, for example, in ferroelectrics [34], but this is optional in materials for transparent electronics, i.e., dielectrics and conductive oxides [35]. A schematic overview of the CSD process is included in Fig. 4.

From the perspective of inkjet printing a typical CSD solution will have a much too low viscosity (usually in the range of only a few mPa) and an almost adequate surface tension, between 20–30 mN m^{-1}, which means its Z value will be around 15–20, i.e., too high. Admixing viscous solvents, such as polyols (PD, ethylene glycol, glycerol (GLY), refer to Table 1), will increase the viscosity of the solvent mixture and thus of the solution. As an example, the changes in the viscosity, surface tension and Z-number of 2-methoxyethanol (2MOE), an often used solvent in CSD, upon the addition of two viscous solvents, PD and GLY, are

shown in Fig. 5. After the addition of the viscous solvent the viscosity steeply increases, which is especially evident in the case of the highly viscous GLY. In parallel, the surface tension of the solvent mixture increases only gradually. As the Z number is proportional to $\sqrt{\gamma}/\eta$, it will decrease with the addition of the viscous solvents (Fig. 5c). CSD solutions are usually diluted, so the behavior of the solvent mixture will be similar to that of the solution [22].
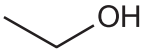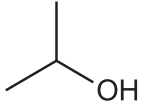
3 Ink–substrate interaction
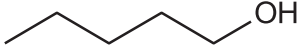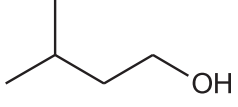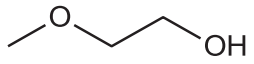
3.1 Drop impact

The principle of inkjet printing is the deposition of liquid drops onto a solid substrate. After the ejection, the drop flies towards the substrate with a velocity between 5 and 20 m s^{-1} [36]. The impact of the drop on the substrate involves five sequential stages: kinematic, spreading, relaxation, wetting, and equilibrium. The first three stages correspond to the impact-driven regime, while the latter two stages correspond to the capillarity-driven regime [37].

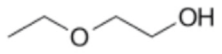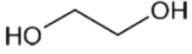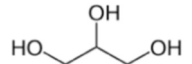In the initial kinematic stage (Fig. 6 I.), the drop obtains the shape of a truncated sphere upon collision with the substrate. At this point, the physical properties of the liquid and the substrate are not important [38]. In the spreading stage (Fig. 6 II.) the drop radially expands. Its spreading is, on the one hand, promoted by the impact velocity and, on the other, hindered by the high surface tension and viscosity. The onset of the relaxation stage (Fig. 6 III.) is marked by the minimum height of the drop and the change of its shape from a flat disk into a spherical cap. In these impact-driven stages (I., II., III.), the drop can undergo several undesired scenarios, such as prompt and corona splash, receding breakup, or partial or complete rebound. These should be avoided in inkjet printing; fortunately, the small size of jetted drops and the ink's fluid characteristics usually prevent their occurrence.

In the wetting stage (Fig. 6 IV.), the capillary forces drive the spreading of a drop until the equilibrium state is reached (Fig. 6 V.). The time scale in capillary-driven stages is much longer than in the impact-driven stages—note that the time in Fig. 6 is plotted on a logarithmic scale. It is important to note that at low contact angles (<90°), the final diameter of the printed drop remains unaffected by the initial impact-driven regime and depends solely on the capillary spreading and wetting. This is exemplified by substrates exhibiting different wetting behaviors: corona-treated (a) or as-received (b) indium-tin-oxide (ITO) coated glass or poly(tetrafluorethylene), PTFE, coated glass (c) shown in Fig. 6. The time required to reach equilibrium is longer for systems with low contact angles (example (a) in Fig. 6) as the drop spreads in proportion to $t^{1/10}$. As

Table 1 Common solvents in CSD, and selected viscous solvents used in ink formulations: viscosity, surface tension and boiling points. If not otherwise specified, the values were obtained from ref. [139]

Component	Skeletal formula	Viscosity mPa s	Surface tension mN m^{-1}	Boiling point °C
SELECTED CSD SOLVENTS				
Methanol		0.54	22.1	65
Ethanol		1.07	22.0	78
2-propanol		2.04	20.9	82
1-butanol		2.54	24.9	118
1-pentanol		3.62	25.4	138
3-methyl-1-butanol		3.69	23.7	131
2-methoxyethanol		1.7	30.8	124
2-ethoxyethanol		2.1	28.4	135
VISCOUS SOLVENTS				
1,3-propanediol [22]		41.8	47.2	215
Ethylene glycol		16.1	48.0	197
Glycerol [22]		828.5	63.1	287

mentioned, the final footprint of a drop is typically independent of the impact-driven regime [39]; thus, the wetting phenomena will be discussed in the subsequent sections.

3.2 Basics of wetting

In the equilibrium stage (Fig. 6 V.) the drop adopts the shape of a spherical cap due to the surface tension. The shape distortions due to gravity are usually negligible [12] and so the shape of the cap is described by the Young–Laplace equation (Eq. 4),

$$\gamma_{sv} = \gamma_{sl} + \gamma_{lv}\cos(\theta_{eq}) \tag{4}$$

where γ_{sv}, γ_{sl}, γ_{lv} are the solid–vapor, solid–liquid, and liquid–vapor interfacial energies. Note that γ_{sv} and γ_{lv} are often referred to as the (solid) surface free energy and (liquid) surface tension, respectively. The equilibrium contact angle between the liquid–vapor interface and the solid surface, θ_{eq}, is a measure of the wetting. For $\gamma_{sv} < \gamma_{sl} + \gamma_{lv}$, the contact angle is 0°, indicating complete wetting. For $\gamma_{sv} = \gamma_{sl} + \gamma_{lv}$, the contact angle is non-zero, resulting in
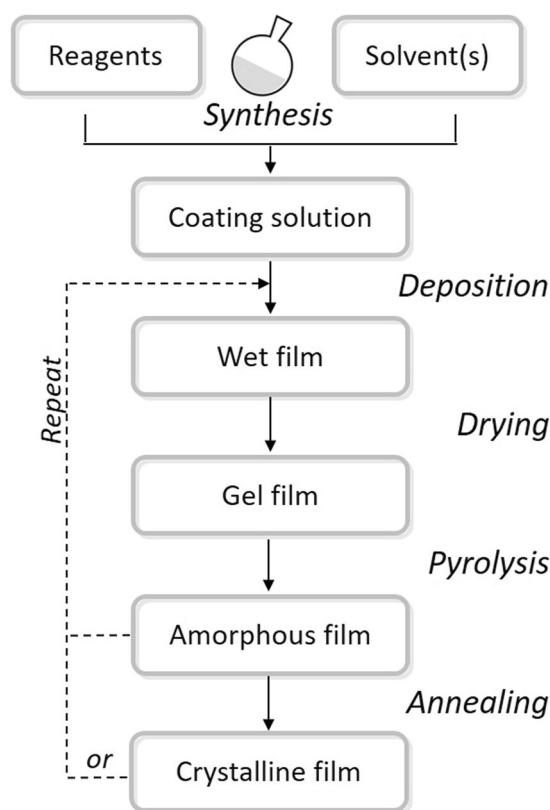
Fig. 4 Schematic representation of the CSD process

Fig. 5 a Viscosity, **b** surface tension and **c** Z number of the 2-methoxyethanol (2MOE)—glycerol (GLY) and 2-methoxyethanol—1,3-propanediol (PD) solvent mixtures. The optimum ranges of viscosity and surface tension, as recommended by the printer producer [3], and the theoretical Z-number range for stable drop formation are given within the horizontal dashed lines. Reproduced with permission from [22]. Copyright 2015, Wiley-VCH

partial wetting. Only γlv can be directly measured, while the evaluation of γ_{sv} and γ_{sl} mainly depends on modeling and is obscured by the contact-angle hysteresis (CAH) (refer to the following section).

Several models have been developed to evaluate γ_{sv}, including Zisman [40], Fowkes [41], Wu [42], Owens–Wendt–Rabel–Kaelble (OWRK) [43–45], van Oss–Good [46], Neumann [47], and more recently also the Marmul-Valal [48] models. The models differ in terms of the type of accounted interactions and the method used to relate them. The OWRK model is quite widely used due to its simplicity and a reasonable agreement with experiments. In brief, the wetting of a given solid surface by a liquid depends on the degree of interactions between the dispersive and polar contributions of the surface free energies of the solid and the liquid. The division of surface interactions into dispersive and polar parts is in place especially when treating liquids and solids of different polarities. The wetting can then be predicted by the wetting diagrams, which consist of wetting envelopes constructed for a given solid surface. Glass and poly(methyl methacrylate), PMMA, are respective examples of a polar surface with a high surface energy and a non-polar surface with relatively low surface energy. According to the OWRK model, the polar contribution of the surface free energy of glass is 91%, and for PMMA it is 23% (Fig. 7) [49]. The contact angles of
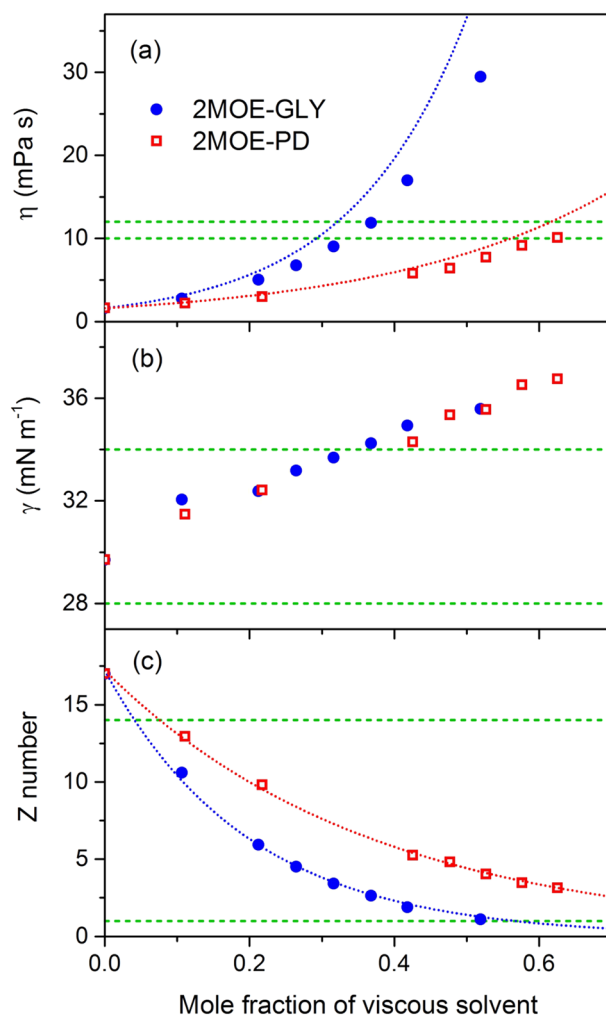
some solvents on glass and PMMA surfaces are collected in Table 2. Ethanol, 2-ethoxyethanol (ether alcohol, similar to, but less toxic than 2MOE), ethylene glycol and formamide wet the glass completely ($\theta \approx 0°$), while GLY and water do not. On the other hand, solvents with a higher surface tension (ethylene glycol, formamide, GLY, and water) exhibit much higher contact angles on the PMMA surface. Ethanol and 2-ethoxyethanol, which are frequently used in the CSD of thin films, completely wet the glass and even the PMMA surfaces. This is favorable in conventional thin-film deposition methods, such as spin coating, but not in inkjet printing. For the latter, the solvents with a higher surface tension and higher contact angles on PMMA are more appropriate. Such solvents can be, in principle, admixed

with solvents that have a lower surface tension to tailor the wetting behavior of the ink.

As an example, the wetting diagrams constructed for glass and PMMA-coated glass substrates are shown in Fig. 7 [49]. The 0°-wetting envelope marks the onset of complete wetting. Inks with the surface-tension contributions lying inside the 0°-wetting envelope wet the surface completely. On the other hand, inks that lie outside the 0° wetting envelope will only partially wet the surface. We note that the wetting is not directly related to the value of the surface energy, but rather depend on the interaction
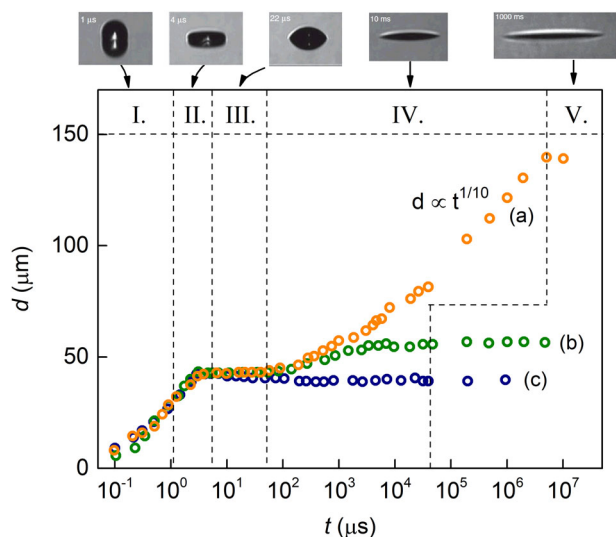

Fig. 6 Time evolution of the drop spreading on a **a** corona-treated ITO-glass, **b** as-received ITO glass, **c** PTFE-coated glass substrates. Figure adapted with permission from [39]. Copyright 2015, Wiley-VCH

between the solid and the liquid. Non-polar liquids (hydrocarbons, benzene, toluene, etc.) typically completely wet non-polar substrates (e.g., PMMA) and partially wet polar substrates (e.g., glass). On the other hand, polar or moderately polar liquids (formamide, ethylene glycol) better wet polar surfaces than non-polar ones, see Table 2. Optical micrographs of the lines on both glass and PMMA that were inkjet printed using two inks with different polarities are included in Fig. 7. It is evident that in the case of a non-polar ink, containing octanol as the main solvent (OCT), the lines printed on a polar surface (glass) will be much narrower than when printed on a non-polar surface and vice-versa.

3.3 Contact angle hysteresis

The Young–Laplace equation (Eq. 4) is only valid for ideal surfaces, which are perfectly smooth, homogenous and chemically inert. In reality, the surfaces exhibit more than just one contact angle. The range of possible contact angles is limited by advancing and receding contact angles. The advancing contact angle, θ_A, is the maximum possible contact angle—the contact line advances when the momentary contact angle exceeds θ_A. The smallest contact angle is the receding contact angle, θ_R, which is the angle at which the contact line starts to recede. The difference between both angles is the CAH, which arises due to the surface imperfections. CAH prevents the drop from sliding on inclined surfaces, such as rain drops resting on windows (Fig. 8a) and has a crucial role in the stability of printed patterns and drying.
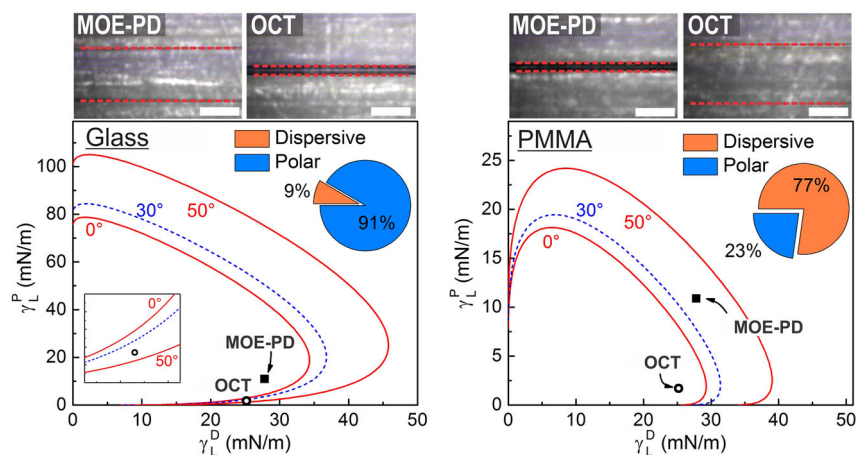
Fig. 7 Top: Optical micrographs of printed lines of two ink formulations of different polarities on glass and PMMA-coated glass substrates. Metal-oxide ink formulations were based on 2-methoxyethanol-1,3-propanediol (MOE-PD) or octanol (OCT) solvents. Red dotted lines in the micrographs mark the edges of the printed lines. Bottom: Wetting diagrams for respective ink formulations on individual substrates. The x and y axes correspond to dispersive ($\gamma_{L,S}^D$) and polar ($\gamma_{L,S}^P$) contributions of the liquid surface tension. Pie charts show the fractions of polar and dispersive contributions to the surface free energy of the solid surfaces. Figure adapted with permission from [49]. Copyright 2016, Royal Society of Chemistry

Table 2 Overall surface tension (Υ) of selected solvents/additives and respective dispersive (γ_L^D) and polar (γ_L^P) contributions

Solvent	Surface tension of a solvent (mJ/m²)				Contact angle on a solid (°)	
	γ	γ_L^D	γ_L^P	Polarity (%)	θ_{PMMA}	θ_{glass}
Ethanol	22.1	17.5	4.6	21	0	0
2-ethoxyethanol	28.6	23.6	5.0	17	0	0
Ethylene glycol	47.7	26.4	21.3	45	50	0
Formamide	57.0	22.4	34.6	61	65	0
Glycerol	63.4	37.0	26.4	42	64	24
Water	72.8	26.4	46.4	64	76	6

The contact angle (Θ) on PMMA and glass is calculated using the OWRK model and surface-energy data from ref. [49] and is in good agreement with experimental measurements
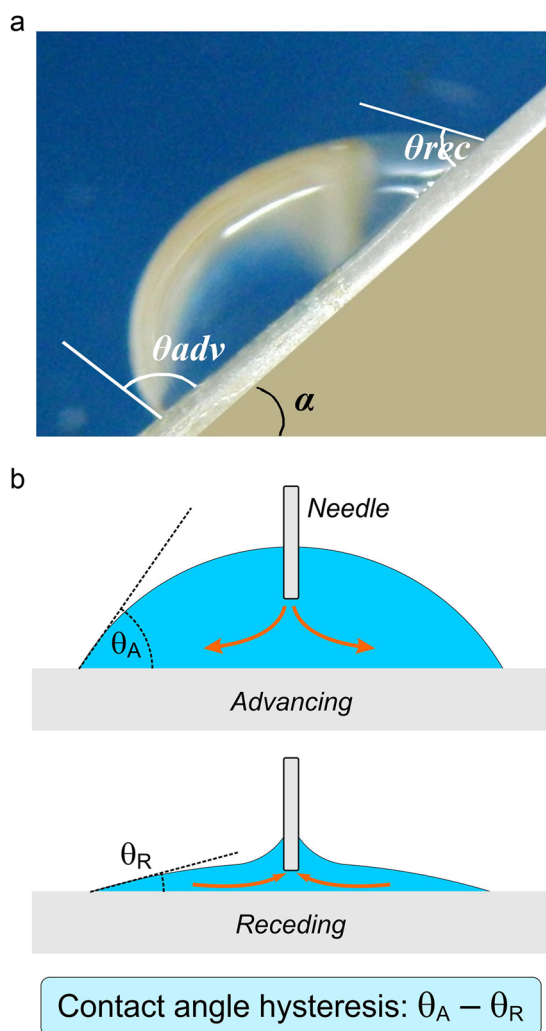

Fig. 8 a A side view of a water drop resting on an inclined surface. Gravitational forces distort the shape of the drop in a way that the contact angle at the bottom is higher than at the top. Reproduced with permission from [137]. Copyright 2016, Elsevier. **b** Captive-drop goniometry: the advancing and receding contact angle can be measured by slowly pumping the liquid in or out of a sessile drop using a needle

The advancing and receding contact angles can be measured using several techniques, including the Wilhelmy plate method [50], the tilted-plate method [51], and captive-drop goniometry [52]. The last of these uses a needle immersed into a sessile drop, while the liquid is slowly pumped in/out of the droplet (Fig. 8b). θ_A is measured by pumping in the liquid and recording the contact angle as a function of the advancing drop diameter. θ_R is determined similarly, but instead, the liquid is pumped out of the drop. The θ_{eq} lies between θ_A and θ_R; it cannot be directly accessed but instead it is estimated from theoretical models (see Ref. [53–57] for more details).

In inkjet printing, the ink–substrate interaction would ideally result in a large θ_A and $\theta_R \approx 0°$. The former is required for high resolution, while the latter is important for the stability of the pattern. However, at high θ_{eq} (and θ_A) the receding contact angle is often nonzero, which negatively affects the pattern's stability. Therefore, both the ink's solvent composition and the substrate should be carefully selected to fulfill these conditions. The CAH greatly depends on the surface properties of the substrate. The CAH increases with the surface roughness and the chemical inhomogeneity of the surface. Topological defects act as pinning sites, which oppose the contact line's movement and enlarge the hysteresis [58]. Additionally, the solute in the ink can promote the pinning of the contact line. This effect is especially pronounced in particle-dispersion inks and less so in solution-based inks. Therefore, it is easier to print well-defined and stable patterns with particle-dispersion inks on rough or chemically inhomogeneous substrates. For printing solution-based inks on smooth substrates (which is often the case), control over the wetting is essential [49]. Special care is needed if the ink consists of more solvents with different wetting properties and volatility. Such inks can, in some cases, exhibit the evaporation-induced wetting transitions [59], resulting in a change of the pattern morphology.

3.4 Manipulation of wetting and spreading of the ink

Wetting and spreading of the ink on a given substrate can be manipulated either by modulating the surface properties of the substrate, or by locally restricting the spreading of the ink. The first approach relies on producing a partial wetting of the substrate. Here, the ink–substrate interaction needs to be well balanced to retain the stability and definition of the printed features. The surface properties of the substrates can be modified by coating them with polymeric layers [49], plasma and corona treatments [60], UV/ozone treatments, or a combination of all these [61, 62].

In the second approach, the spreading of the ink is locally limited by surface-energy patterning [63]. Such patterns

consist of low-surface-energy materials, such as self-assembled monolayers (SAMs), polymers, and siloxane. The approach exploits the ink-repelling nature of the surface-energy pattern, which forces the ink into the uncovered areas. The contact angle of the uncovered areas should be small to promote the spreading and stability of the pattern. Such patterns can be deposited by lithography-based processes, micro-contact printing [63], shadow-mask-assisted plasma treatment [64], and also inkjet printing.

Thin-film transistors with the channel layer width beyond the resolution of conventional inkjet printing provide an interesting case of local wetting manipulation. Wang et al. [65] used lithography to pattern the lines of per-fluorodecyltrichlorosilane—a non-polar, low-surface-energy material [66]. The inkjet printing of aqueous polymer solutions on such lines resulted in de-wetting of the droplets in the areas of SAMs. Such an approach enabled the fabrication of self-aligned source and drain electrodes in a thin-film transistor with a resolution as low as 250 nm. The same authors later reported the selective functionalization of a printed layer so that it repelled the next printed layer, resulting in sub-100-nm gaps between both layers [67]. In a more general approach, Li et al. exploited the "coffee stain" effect for patterning. The inkjet-printed polymer-based ink formed approximately 3.5-μm wide edge deposits, which acted as ink-repelling stripes upon deposition of the functional material.

3.5 Stability of printed features

Printed devices and circuits usually consist of structures of different shapes, such as dots, lines or rectangles. While the printing of individual drops is straightforward, the printing of lines and rectangles requires individual drops to partially overlap and coalesce. The drop spacing, which is the distance between the centers of adjacent drops, also indicates the degree of overlap together with the drop size. Individual drops are always stable, while complex structures can exhibit instabilities. In 1980, Davis [68] investigated the stability of static rivulets as a function of the contact angle. He postulated that the ultimate conditions for a stable liquid bead included a contact angle smaller than 90° and a fixed contact line ($\theta_R = 0$). Both conditions have been subsequently experimentally validated [69]. Upon printing the lines with inks having a zero receding contact angle, periodically repeating bulges can appear [8, 69]. Duineveld [8] studied the bulging using a dynamic model and found that bulges occur when the momentary contact angle exceeds the advancing contact angle and the transported flow rate becomes larger than the applied flow rate. Consequently, a small drop spacing, a low deposition rate, and a high advancing contact angle promote the occurrence of bulging.

Several papers discuss the limits of line stability in terms of drop spacing and deposition rate for liquids with a zero receding contact angle. Soltman and Subramanian [70] investigated the printing of the lines across a range of drop spacings, deposition rates, and substrate temperatures, see Fig. 9a. For a drop spacing of twice the drop diameter or more the drops fail to coalesce and remain separated. Decreasing the drop spacing so that there is barely any overlap between drops produces lines with scalloped edges. An even smaller drop spacing results in narrow and stable lines with parallel edges, but if it is further reduced the bulging develops. Stringer and Derby [7] investigated the line stability at the onsets of scalloping and bulging. They reformulated the Duineveld model and mapped the regions of stability as a function of dimensionless print velocity, contact angle, and drop spacing. It is clear that the attainable line width has an upper and a lower boundary. Bulging and scalloping respectively limit the largest and smallest widths of a printed line for a given contact angle [71].

The above analysis is valid for systems with pinned contact lines. Recently, Hsiao et al. [72] investigated the formation of liquid beads in a system with a non-zero receding contact angle, where the dynamics of line formation is also important. They used high-speed imaging to follow the coalescence of drops and liquid flow during the deposition on the substrate, see Fig. 9b. Stable and relatively symmetrical lines formed at large drop spacings and short deposition times.

In conventional inkjet printing 2D patterns are formed using a raster-scan technique. For example, a rectangular pattern is formed by printing individual lines in the x-direction and offsetting them in the y-direction (Fig. 10a). Kang et al. [73] investigated the morphology of printed rectangular structures as a function of drop spacing. The printed 2D patterns exhibited essentially the same morphologies as printed lines. As shown in Fig. 10b, a large drop spacing prevented the coalescence of drops. Bulging occurred when the drop spacing was too low and the momentary contact angle exceeded the advancing contact angle.

The square-shaped patterns have much lower aspect ratios than the lines, and can remain continuous even at a nonzero receding contact angle. However, rounding of the corners occurs when the contact line is not pinned. Soltman et al. [74] demonstrated the evolution of a square morphology with increasing CAH (Fig. 10c). At a small hysteresis, the printed square-shaped pattern exhibited rounded edges and resembled a large drop. The rounding of the edges decreased with increasing hysteresis until squares with sharp edges formed; note that the diameter of an individual drop sets the edge curvature of a square pattern. A large CAH—or more precisely, a zero or small receding
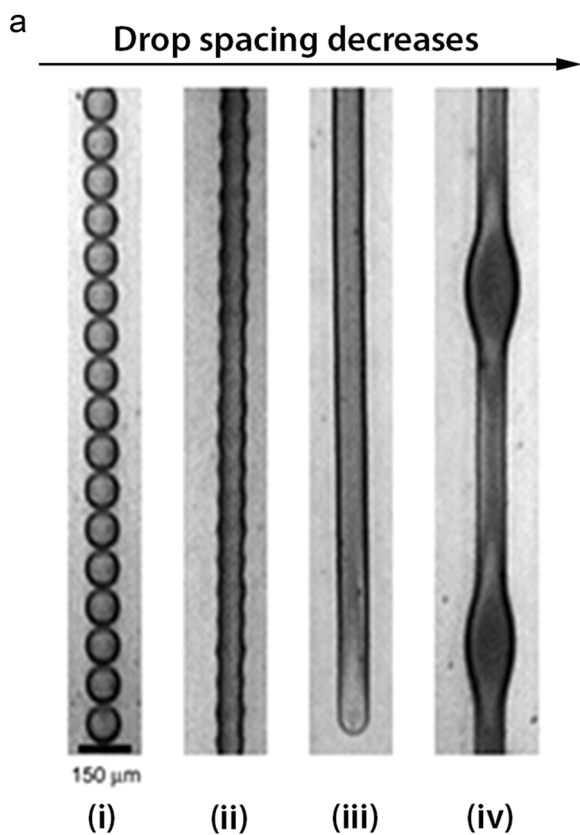
a

Drop spacing decreases →

150 μm

(i)   (ii)   (iii)   (iv)

b

+ 1.3 s   + 31.5 ms

Δx = 130 μm   Δx = 130 μm
Δt = 40 ms   Δt = 1 ms

Fig. 9 a Basic morphologies of printed lines depending on the drop spacing: (i) separated drops, (ii) scalloping, (iii) uniform, (iv) bulging. Figure adapted with permission from [70]. Copyright 2008, American Chemical Society. **b** Dynamics of liquid track formation at two different deposition intervals. When the time between the depositions of consecutive drops is large, the drops coalesce before the deposition is complete (shown on the left-hand side). The pressure difference due to different curvatures causes the liquid flow from a newly deposited drop to the existing bead of liquid. At short deposition intervals, all the drops remain separated during the whole deposition process (right-hand side). After some time the drops merge due to the capillary spreading and form a liquid bead. Figure adapted with permission from [72]. Copyright 2014, American Chemical Society
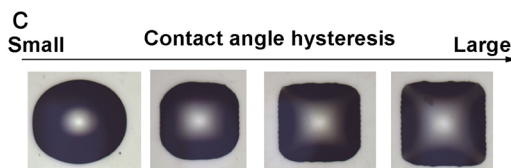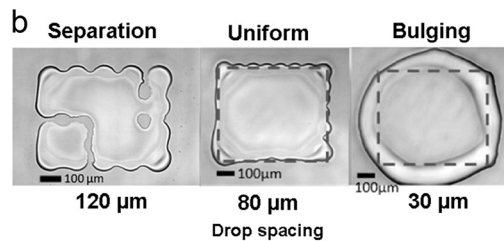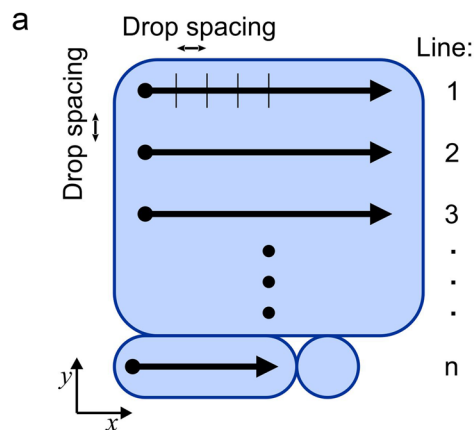
a

Drop spacing

Line: 1, 2, 3, ... n

b

Separation   Uniform   Bulging

120 μm   80 μm   30 μm

Drop spacing

c

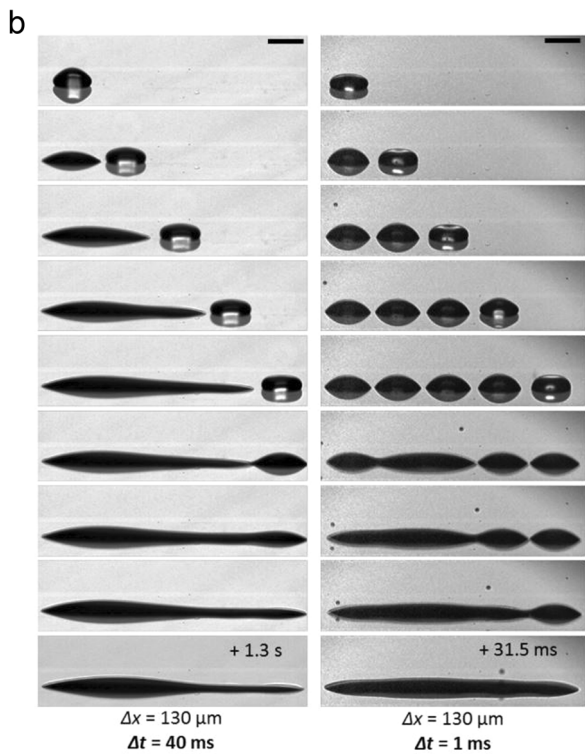Small   **Contact angle hysteresis**   Large →

Fig. 10 a Formation of a 2D pattern using a raster-scan technique. Figure adapted with permission from [74]. Copyright 2013, Elsevier. **b** Possible instabilities for 2D patterns. The dotted line shows the desired shape of the 0.5×0.5 mm^2 square. Figure adapted with permission from [73]. Copyright 2010, American Chemical Society. **c** Influence of contact-angle hysteresis on the morphology of printed 1×1 mm^2 squares. Figure adapted with permission from [74]. Copyright 2013, Elsevier

contact angle—is essential for printing well-defined 2D patterns with sharp edges.

Thus far, we have only discussed single-solvent inks. In inks containing several solvents with different volatilities and surface tensions, the wetting and the stability of printed patterns can be functions of time. Evaporation of more volatile solvent(s) already in the course of the printing leads to changes in the ink formulation, which consequently

results in a different wetting behavior. While the printing of lines is relatively fast, the printing of 2D patterns is more time-consuming. The ink that contained two solvents with different boiling points and surface tensions, such as 2MOE and PD (refer to Table 1), produced well-defined 2D patterns, while according to the contact-angle measurements such an ink should exhibit complete wetting and thus spilling. This inconsistency was explained in terms of the preferential evaporation of the more volatile solvent during the raster-scan printing of a 2D pattern [49]. Another consequence of such a preferential evaporation is increased solute concentration in the ink, which can contribute to contact-line pinning. Thus, optimization of the printing parameters often relies on experimental trials.

4 Drying and consolidation

After the printing step, the as-deposited pattern is dried and usually heated to transform the organic precursor into a functional oxide. During drying, the solvents evaporate and the concentration of the solute in the deposit gradually increases. This results in an increase in viscosity until the sol–gel transition. In contrast to spin coating, where uniformly thick films are typically prepared [33], the drying of inkjet-printed structures often results in a non-uniform thickness. In fact, the deposition of uniformly thin structures is one of the challenges for the inkjet printing of functional materials. Further heating steps do not introduce major changes to the shape of the printed pattern.

The so-called coffee-stain effect refers to the evolution of a ring-like thickness profile of a deposit upon drying (Fig. 11). Deegan et al. [11, 75] showed that it is a consequence of the preferential evaporation at the edge of the drying feature and pinning of the contact line. The combination of both phenomena results in an internal liquid flow from the interior to the edge to replenish the evaporated solvent. The associated transport of the solute due to the capillary flow eventually builds up the deposit at the edges.

Several strategies have been developed to eliminate or minimize the coffee-stain effect. The simplest way to suppress the edge-deposit formation is to eliminate the contact line pinning or preferential edge evaporation. The de-pinned contact line leads to the dome-shaped deposit with a much smaller diameter than the initial drop size. The inward motion of the contact line has been exploited in the self-assembly of colloidal spheres [76]. But due to the unpinned contact line (non-zero contact angle) the method is mainly limited to the printing of individual drops. The deposit's uniformity can also be improved by retarding the evaporation from the edges of a drying feature [77, 78]. Berg et al. [79] exploited a temperature-induced gelation of a polymer to freeze the shape of a printed pattern before drying could produce a coffee
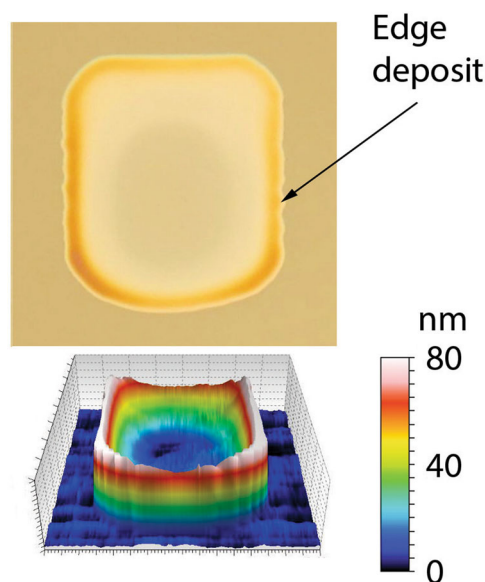

Fig. 11 The left-hand figure shows a stain of coffee spilled and dried on a surface. A similar morphology often occurs when the inkjet-printed pattern dries, as shown in the optical micrograph and the corresponding thickness profile on the right

stain. Similarly, Talbot et al. [80] studied the drying of laponite dispersions, which exhibit a strong increase in viscosity with the increasing concentration of the solute.

4.1 Multi-solvent inks

A common approach to reducing coffee-stain formation is by inducing a surface-tension gradient across the drying structure, which results in a recirculating Marangoni flow [81]. Such a gradient is produced by thermal fluctuations [81], added surfactants [82, 83], or a variation in composition [9]. The most convenient approach to induce the Marangoni flow in solution-based inks is a combination of solvents. Typically, such inks consist of two or more solvents with different viscosities, surface tensions, and vapor pressures. The enhanced evaporation from the edge of the drying feature leads to local depletion of a more volatile solvent. The surface-tension gradient induces the Marangoni flow. As opposed to the directional capillary flow, the Marangoni flow is recirculating and is able to intensively mix the content of the drop in the course of drying (Fig. 12a). The temporal evolution of the internal liquid flows upon drying thus depends on the ink's composition, the ambient conditions and the substrate's properties. Some of the parameters that influence the drying of solution-based inks are collected in Fig. 12b.

The multi-solvent approach has been used to improve deposit uniformity in particle-dispersion inks [84, 85], polymer-solution inks [9, 86, 87], and metal-oxide precursor-solution inks [22, 61, 88]. In a study relevant to solution-based inks, Kajiya et al. [89] used fluorescence
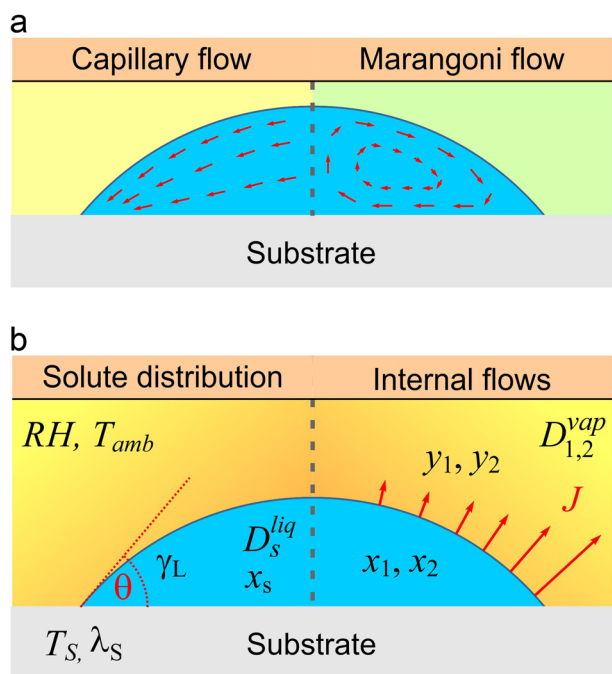
Fig. 12 Schematic representation of a drop cross-section upon drying. **a** The comparison of capillary and Marangoni flows. **b** Selected variables that influence the morphology of a deposit. x_1, x_2, y_1, y_2 are the fractions of solvents 1 and 2 in the liquid and vapor phase, $D_{1,2}^{vap}$ is the diffusion coefficient of the solvents in the vapor phase, D_s^{liq} is the diffusion coefficient of the solute in the liquid phase, x_s is the solute concentration, γ_L is the surface tension of the ink, θ is the contact angle, T_S and the T_{amb} are the temperatures of the substrate and air, respectively, λ_S is the thermal conductivity of the substrate, RH is the relative humidity of air

microscopy to follow the spatial concentration of fluorescent polystyrene dissolved in anisole upon drying. They observed a gradual increase in the solute concentration at the edge, eventually leading to a ring-like deposit. The morphology of a deposit depends on the choice of the solvents, their relative fractions in the ink [22, 86], solute concentration [90], drop spacing [61, 91], drying temperature [92, 93] and wetting [94], as well as the air humidity [95], the temperature of the substrate [70, 96], and the local environment [77, 97–99]. Some examples of the influence of selected parameters on the morphology of a dried deposit are collected in Fig. 13.

Recently, Diddens et al. [59, 100] developed a mathematical model to describe the drying of binary-solvent sessile drops based on a lubrication approximation. They demonstrated the preferential evaporation of a more volatile solvent and showed that the surface-tension-driven flow typically vanishes before the drying is complete. This is in agreement with experimental studies [22] and implies that the late stages of drop evaporation might be important for the final morphology of a deposit, especially in solution-based inks.

4.2 Drying of 2D geometrical shapes and patterns

In a recent study Sáenz et al. [101] showed that the drying of geometrically complex structures with non-spherical symmetry is somewhat different from the drying of axially symmetric features. Whereas symmetrical deposits have a constant contact angle along the whole liquid–solid
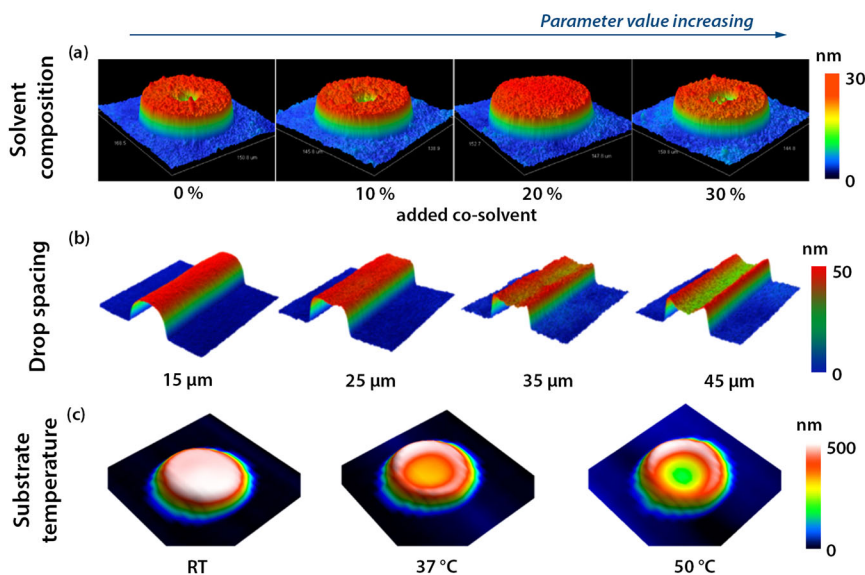
Fig. 13 a 12-nm-diameter quantum-dot dispersion ink in cyclohexylbenzene with 0, 10, 20, 30% 1,2-dichlorobenzene. Figure adapted with permission from [138]. Copyright 2016, American Chemical Society. **b** Indium and gallium nitrate solution ink in 2-methoxyethanol with 50 vol.% ethylene glycol. Lines were printed at different drop spacings. Figure adapted with permission from [91]. Copyright 2017, American Chemical Society. **c** Epoxy solution ink in cyclopentatone with 20 wt.% of added γ-butyrolactone dried at different temperatures. Figure adapted with permission from [93]. Copyright 2015, American Chemical Society

Fig. 14 Simulations of the local evaporation flux for patterns with **a**, **b** circular and **c**, **d** triangular geometries. Figure adapted with permission from [101]. Copyright 2017, Springer Nature

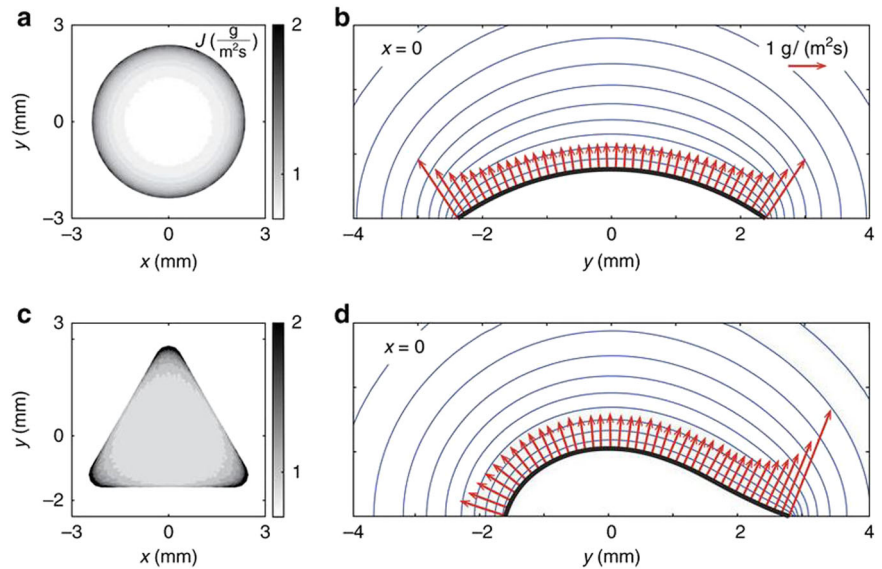**Fig. 15** Schematic representation of vapor fields during the drying of an individual square and an array of squares. **b** Optical image of the edge part of an array of dried squares. The darker color at the edge of the outer squares corresponds to a thicker deposit. **c** The morphology of two drops dried adjacent to each other. Figure adapted with permission from [99]. Copyright 2010, The Physical Society of Japan
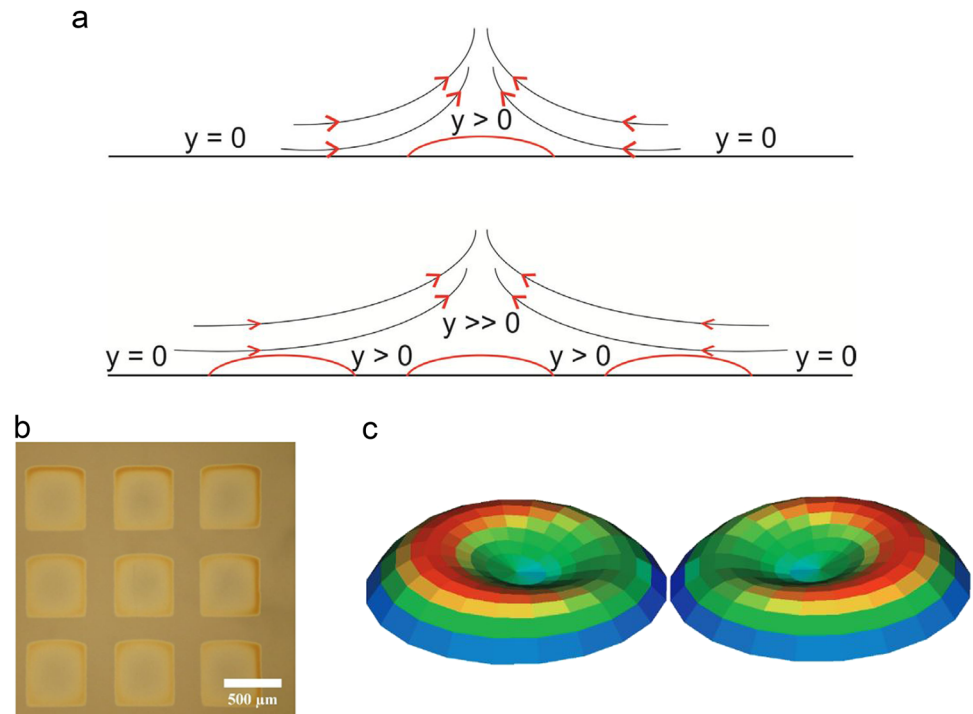
interface this is not the case in patterns with a broken symmetry. A triangular feature has higher and lower contact angles at the sides and at the corners, respectively. This results in the enhanced evaporation in the corners of the structure and hence a stronger capillary flow to these regions. Thus, the deposit height will be higher in the corners than at the sides of a triangular feature. Other geometries follow the same basic principle Fig. 14.

The printing pattern often consists of several features or arrays in proximity to each other. The evaporation fields of two neighboring features can overlap if they are sufficiently close, which interferes with the drying process (Fig. 15a).

Consequently, the evaporation flux is reduced and the capillary flow to that area is weaker. In practice, the overlap of evaporation fields results in a smaller deposit height at adjacent sites (Fig. 15b, c). The phenomenon has been analytically and experimentally studied by Kobayashi et al. [99], Hu et al. [98], and Tao et al. [97].

5 Materials, applications and outlook

The rich variety of electrical and optical properties of metal oxides makes them the materials of choice in printed

electronics, ranging from conventional electronic components to sophisticated devices with new functionalities. Printed electronic devices typically consist of conductive and dielectric layers in metal–insulator–metal (MIM), or a planar configuration. A representative example of a MIM component is a thin-film capacitor (TFC), where a dielectric layer is sandwiched between the top and bottom electrodes (Fig. 16a). In the planar configuration, the electrodes are interdigitated and fully embedded with the functional material or placed on top of it (Fig. 16b). Such a configuration is particularly suitable for chemical sensors, where the high surface area of the functional layer is essential for the device's performance. Some electronic devices use both configurations for their operation, such as thin-film field-effect transistors, in which the out-of-plane electric field modulates the in-plane conductivity of the channel layer. We note that only rare reports of fully printed components or devices exist, as such an approach requires the deposition of multiple overlapping layers.

In the field of transparent electronics, optically transparent electrical devices are obtained by depositing conductive and dielectric layers on transparent substrates, usually glass [35]. Due to the specific requirements an amorphous structure of metal oxides is desired. Jang et al. [61] reported fully printed TFTs on glass using SnO_2:Sb as the electrodes, SnO_2 as the semiconductor and ZrO_2 as the dielectric. TFTs were transparent in the visible-light spectrum and exhibited good electrical properties. To regulate the wetting during the fabrication process they used a thin coat of PMMA and subsequent UV/O_3 treatment. Similarly, Zeumault et al. [102] fabricated fully printed TFTs on flexible polyimide substrates at a maximum temperature of 300 °C. Again, the TFTs were transparent; however, they exhibited rather poor electrical properties, presumably due to the low processing temperature and the cracking. Li et al. [91] fabricated fully printed TFTs with excellent optical and electrical properties. Matavž et al. [19] fabricated TFCs on glass consisting of indium-zinc oxide (IZO) electrodes and a tantalum-oxide-based dielectric. The TFCs processed at 450 °C were transparent and had good electrical properties comparable to those of spin-coated high-K dielectric thin films of the same chemical composition [103]. Vescio et al. [104] fabricated flexible TFCs on polyimide substrates with hafnium-oxide-based dielectric and metal electrodes deposited from a silver-nanoparticle ink.

More often, inkjet printing has been used in combination with other deposition methods to fabricate the device. The common materials include zinc oxide [105], indium oxide [106–108], and tin oxide [61], or mixed oxides, such as indium-zinc oxide [19, 21], indium-tin oxide (ITO) [109–111], indium-gallium-zinc oxide (IGZO) [112, 113], indium-zinc-tin oxide (IZTO) [114, 115], zinc-tin oxide (ZTO) [92, 116], aluminum-zinc oxide (AZO) [117], and others. In both, TFTs and TFCs, the dielectric should exhibit a large breakdown field, low leakage current density, a large dielectric permittivity and good interface with other materials. Furthermore, the dielectric layer should be flat and uniform to ensure a uniform electric field distribution [118]. Reports on the printed metal oxide dielectrics include tantalum oxide [22], zirconium oxide [91], aluminum oxide [119], and silicon oxide [120].

Ferroelectrics are widely used in electronic and electromechanical applications, for example, in non-volatile ferroelectric random-access memories (FeRAMs), ceramic resonators, ultrasonic transducers and actuators, energy harvesters, ferroelectric capacitors, etc. Machida et al. [121] used a combination of surface-energy patterning of the substrate by SAMs and inkjet printing to prepare patterned lead zirconate titanate (PZT) films on platinized silicon substrates. By repeating the printing process, the authors prepared ≈2-μm-thick PZT films with (111) orientation and functional properties comparable to spin-coated films. The ink was obtained by adding a high-boiling-point solvent to a 2-MOE-based coating solution; however, further experimental details were not reported. The thickness non-uniformity of the structures that developed as a
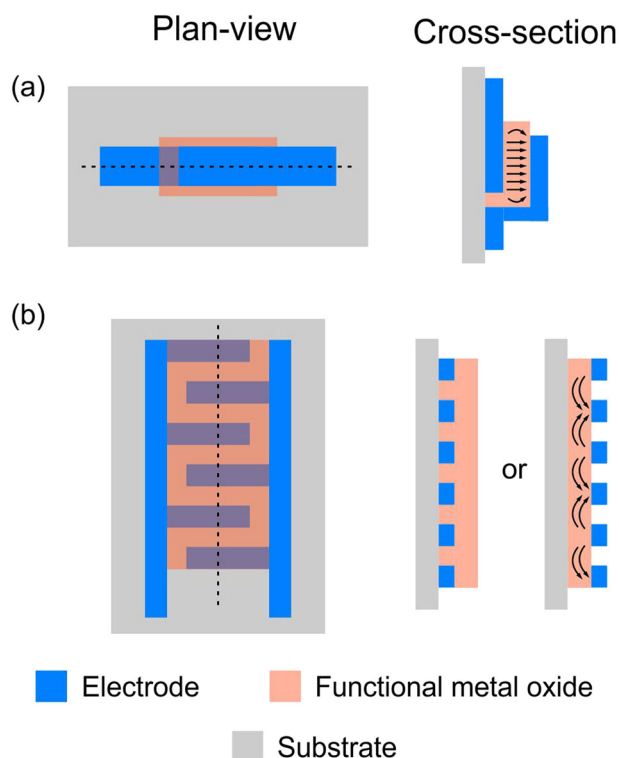

Fig. 16 Plan-view and cross-sectional view of the electronic components with **a** metal-insluator-metal and **b** planar configuration. The dotted lines in plan-view show the cut for the cross-sectional view. Arrows in the cross-sectional view show the electric field propagation in these devices. The dimensions in the cross-sectional view are exaggerated for better presentation

consequence of the coffee-stain effect was avoided by reducing the heating-rate. The authors reported that dielectric and ferroelectric properties of the inkjet printed and spin-coated films, both crystallized at 700 °C, were comparable. Bathurst and Kim [88] printed uniform PZT structures on platinized silicon by adapting commercially available PZT precursor solutions. The 700-nm-thick PZT layer formed after repeating the printing/annealing process 22 times. In combination with the etching process, they prepared a micro-machined ultrasonic transducer (pMUT) with good functional performance [122].

Kaydanova et al. [123] inkjet-printed barium strontium titanate on MgO substrates with thicknesses between 280 and 420 nm by repeating deposition, pyrolysis, and annealing steps. They fabricated tunable ferroelectric capacitors (varactors) with planar interdigitated electrodes by a combination of spray coating silver layer and lithography process. They observed that the grain size, dielectric permittivity, and its voltage tunability increased with film thickness, thus following the trend reported for spin-coated films [124]. List et al. [125] successfully printed filaments of superconducting $YBa_2Cu_3O_7$ on Ni–W tapes. Later, Feys et al. [126] demonstrated the deposition of superconducting coatings of $YBa_2Cu_3O_7$ on strontium titanate single-crystal substrates and Ni–W tapes by inkjet printing metal–salt aqueous solutions. About 200-nm-thick, flat and uniform tracks of superconductors with a strong c-axis orientation were obtained. Other reports on inkjet-printed functional oxide materials include Y_2O_3-stabilized ZrO_2 [127], $NiCo_2O_4$ [128], and $Ce_{0.8}Gd_{0.2}O_2$ [129, 130] for applications in solid-oxide fuel cells (SOFCs), NiO_x [131, 132] layers for applications in solar cells, and optically active phosphors $YVO_4:Eu^{3+}$ [133], $Zn_2SiO_4:Mn^{2+}$, and $Y_2SiO_5:Eu^{3+}$ [134].

Functional properties and some potential applications of printed metal-oxide thin films are collected in Fig. 17. We note that inkjet printing as almost every technology or processing technique leaves an imprint in a material which is then reflected in its functional properties. In inkjet printing macroscopic defects such as thickness non-uniformity of the printed patterns due to the coffee-stain effect may be detrimental for functional properties, for example, distribution of the electric field will be non-uniform in a MIM TFC [118]. On nano-scale and micro-scale the fraction and size distribution of porosity, presence/absence of long-range order (crystallinity), grain size and shape, chemical homogeneity influence the functional properties. To our knowledge, detailed studies which would relate microstructural details with specific functional properties of inkjet printed (nano-)structures have not been performed yet. Although the fabrication of printed devices is challenging due to the highly interdisciplinary nature of the process, the very same problems create room for innovative approaches and the fabrication of innovative devices and concepts. Good examples include printed hierarchical silver-wire circuits [135] or self-aligned channels with resolution in the sub-100-nanometer range [67].

The inkjet printing of sol–gel inks enables integration of different materials, including functional oxides and metals without additional lithography steps. It is also an exciting alternative to miniaturization of functional oxides to nanoscale by various bottom-up templating methods which are typically quite complex [136]. The apparent simplicity of inkjet printing is nevertheless challenged when considering fabrication of uniform multi-component (nano-)structures with precise and uniform dimensions. Clearly, understanding of the fluid properties of either solution-dispersion or nanoparticle-dispersion based inks is one of the crucial requirements. For example, keeping the thickness uniformity of a printed pattern in nanometer range requires the ability to understand and control the coffee-stain effect in the process of drying.

Fig. 17 Schematic representation of selected functional properties of metal oxides and possible applications
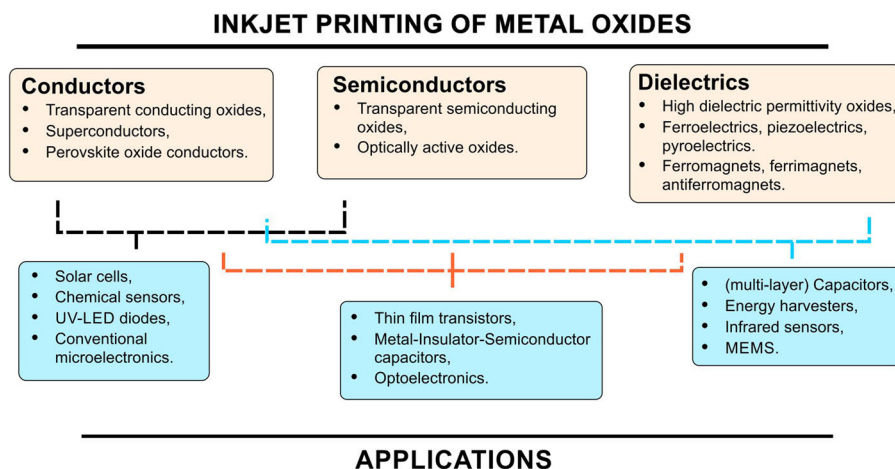
On the other hand, the ink formulation determines not only its interaction with the substrate—and is consequently important in the planning of lateral dimensions of a given pattern—but also the consolidation. The potential outreach of inkjet printing of functional oxides is in low-cost electronics, which implies temperature-sensitive substrates, such as polymer foils, paper, or textile. Low-temperature or non-thermal processing, such as UV activation, enables consolidation of functional oxides on such substrates, but also requires a specific ink chemistry, such as incorporating UV-sensitive species.

An exciting challenge is inkjet printing of 3-dimensional (3D) structures; that is, the fabrication of fully printed components or devices. In order to make such process feasible the current paradigm of ink formulation should be reconsidered. Namely, solution-based inks are typically quite diluted, which on one side allows the control of sol–gel reactions but on the other hand implies numerous time-consuming steps of printing and drying/consolidation resulting also in a possible loss of dimensional accuracy. But, once understood and mastered, it would enable fabrication of miniature devices for numerous application fields, like sensors, MEMS, displays, photovoltaics, or batteries.

6 Summary

The inkjet printing of functional oxides is a direct writing technique that enables the integration of different materials into electric components or devices without additional fabrication steps. Upon printing, the pattern gradually forms by placing ejected droplets of ink onto a substrate. In contrast to lithography the inkjet printing process is digitally controlled and does not require the use of masks, which gives a flexibility to the pattern design. Printing appears to be a ubiquitous technology; nevertheless, it presents many challenges related to the printing process, which is even more evident when printing functional oxide nanostructures planned for use in electronics, photovoltaics, telecommunications, or sensorics. For example, thickness uniformity within nanometre range over lateral dimensions extending over several micrometers or millimeters is crucial in some applications. Such and similar issues can be successfully addressed by understanding the interplay between the ink formulation—its chemical composition and physical properties, the interaction of the ink with the substrate, and the control over the consolidation of the printed pattern.

Compliance with ethical standards

Conflict of interest The authors declare no conflict of interest.

References

1. Hudd A (2009) Inkjet printing technologies. In: Magdassi S (ed) The chemistry of inkjet inks. World Scientific, Singapore, pp 3–18
2. Morita N, Khalate AA, Buul AM, Wijshoff H (2015) Inkjet printheads. In: Hoath SD (ed) Fundamentals of inkjet printing. Wiley-VCH Verlag GmbH & Co. KGaA, Weinheim, Germany, pp 57–92
3. Dimatix Fujifilm. Jettable Fluid Formulation Guidelines. https://www.fujifilmusa.com/shared/bin/Dimatix-Materials-Printer-Jettable-Fluid-Formulation-Guidelines.pdf. Accessed 14 Jul 2016
4. Driessen T, Jeurissen R (2015) Drop formation in inkjet printing. In: Hoath SD (ed) Fundamentals of inkjet printing. Wiley-VCH Verlag GmbH & Co. KGaA, Weinheim, Germany, pp 93–116
5. Magdassi S (2009) Ink requirements and formulations guidelines. In: Magdassi S (ed) The chemistry of inkjet inks. World Scientific, Singapore, pp 19–41
6. Reis N, Derby B (2000) Ink jet deposition of ceramic suspensions: modeling and experiments of droplet formation. MRS Proc 625:117–122. https://doi.org/10.1557/PROC-625-117
7. Stringer J, Derby B (2010) Formation and stability of lines produced by inkjet printing. Langmuir 26:10365–10372. https://doi.org/10.1021/la101296e
8. Duineveld PC (2003) The stability of ink-jet printed lines of liquid with zero receding contact angle on a homogeneous substrate. J Fluid Mech 477. https://doi.org/10.1017/S0022112002003117
9. Tekin E, de Gans B-J, Schubert US (2004) Ink-jet printing of polymers from single dots to thin film libraries. J Mater Chem 14:2627–2632. https://doi.org/10.1039/b407478e
10. Sun J, Bao B, He M et al. (2015) Recent advances in controlling the depositing morphologies of inkjet droplets. ACS Appl Mater Interfaces 7:28086–28099. https://doi.org/10.1021/acsami.5b07006
11. Deegan RD, Bakajin O, Dupont TF et al. (1997) Capillary flow as the cause of ring stains from dried liquid drops. Nature 389:827–829. https://doi.org/10.1038/39827
12. Derby B (2010) Inkjet printing of functional and structural materials: fluid property requirements, feature stability, and resolution. Annu Rev Mater Res 40:395–414. https://doi.org/10.1146/annurev-matsci-070909-104502
13. Derby B (2015) Additive manufacture of ceramics components by inkjet printing. Engineering 1:113–123. https://doi.org/10.15302/J-ENG-2015014
14. Singh M, Haverinen HM, Dhagat P, Jabbour GE (2010) Inkjet printing-process and its applications. Adv Mater 22:673–685. https://doi.org/10.1002/adma.200901141
15. Das RN, Lin HT, Lauffer JM, Markovich VR (2011) Printable electronics: towards materials development and device fabrication. Circuit World 37:38–45. https://doi.org/10.1108/03056121111101278
16. de Gans B-J, Duineveld PC, Schubert US (2004) Inkjet printing of polymers: state of the art and future developments. Adv Mater 16:203–213. https://doi.org/10.1002/adma.200300385
17. Fromm JE (1984) Numerical calculation of the fluid dynamics of drop-on-demand jets. IBM J Res Dev 28:322–333. https://doi.org/10.1147/rd.283.0322

18. Kuscer D, Stavber G, Trefalt G, Kosec M (2012) Formulation of an aqueous titania suspension and its patterning with ink-jet printing technology. J Am Ceram Soc 95:487–493. https://doi.org/10.1111/j.1551-2916.2011.04876.x

19. Matavž A, Malič B, Bobnar V (2017) Inkjet printing of metal-oxide-based transparent thin-film capacitors. J Appl Phys 122:214102. https://doi.org/10.1063/1.5000432

20. Jang D, Kim D, Moon J (2009) Influence of fluid physical properties on ink-jet printability. Langmuir 25:2629–2635. https://doi.org/10.1021/la900059m

21. Tellier J, Malic B, Kuscer D et al. (2011) Ink-jet printing of In2O3/ZnO two-dimensional structures from solution. J Am Ceram Soc 94:2834–2840. https://doi.org/10.1111/j.1551-2916.2011.04425.x

22. Matavž A, Frunză RC, Drnovšek A et al. (2016) Inkjet printing of uniform dielectric oxide structures from sol–gel inks by adjusting the solvent composition. J Mater Chem C 4:5634–5641. https://doi.org/10.1039/C6TC01090C

23. Vernieuwe K, Feys J, Cuypers D, De Buysser K (2016) Ink-jet printing of aqueous inks for single-layer deposition of Al-doped ZnO thin films. J Am Ceram Soc 99:1353–1359. https://doi.org/10.1111/jace.14059

24. Schwartz RW, Schneller T, Waser R (2004) Chemical solution deposition of electronic oxide films. Comptes Rendus Chim 7:433–461. https://doi.org/10.1016/j.crci.2004.01.007

25. Schneller T, Waser R, Kosec M, Payne D (eds) (2013) Chemical solution deposition of functional oxide thin films. Springer Vienna, Vienna

26. Bassiri-Gharb N, Bastani Y, Bernal A (2014) Chemical solution growth of ferroelectric oxide thin films and nanostructures. Chem Soc Rev 43:2125–2140. https://doi.org/10.1039/C3CS60250H

27. Schneller T (2013) Simple alkoxide based precursor systems. In: Schneller T, Waser R, Kosec M, Payne D (eds) Chemical solution deposition of functional oxide thin films. Springer Vienna, Vienna, pp 3–28

28. Schneller T, Griesche D (2013) Carboxylate based precursor systems. In: Schneller T, Waser R, Kosec M, Payne D (eds) Chemical solution deposition of functional oxide thin films. Springer Vienna, Vienna, pp 29–49

29. Malič B, Glinšek S, Schneller T, Kosec M (2013) Mixed metallo-organic precursor systems. In: Schneller T, Waser R, Kosec M, Payne D (eds) Chemical solution deposition of functional oxide thin films. Springer Vienna, Vienna, pp 51–69

30. Kim SJ, Kim GH, Kim DL et al. (2010) InGaZnO thin-film transistors with YHfZnO gate insulator by solution process. Phys Status Solidi Appl Mater Sci 207:1668–1671. https://doi.org/10.1002/pssa.200983724

31. Street RA, Ng TN, Lujan RA et al. (2014) Sol − gel solution-deposited InGaZnO thin film transistors. https://doi.org/10.1021/am500126b

32. Tu Y-L, Calzada ML, Phillips NJ, Milne SJ (1996) Synthesis and electrical characterization of thin films of PT and PZT made from a Diol-based sol-gel route. J Am Ceram Soc 79:441–448. https://doi.org/10.1111/j.1151-2916.1996.tb08142.x

33. Birnie DP (2013) Spin coating: Art and science. In: Schneller T, Waser R, Kosec M, Payne D (eds) Chemical solution deposition of functional oxide thin films. Springer Vienna, Vienna, pp 263–274

34. Schwartz RW, Narayanan M (2013) Thermodynamics and heating processes. In: Schneller T, Waser R, Kosec M, Payne D (eds) Chemical solution deposition of functional oxide thin films. Springer Vienna, Vienna, pp 343–382

35. Fortunato E, Barquinha P, Martins R (2012) Oxide semi-conductor thin-film transistors: a review of recent advances. Adv Mater 24:2945–86. https://doi.org/10.1002/adma.201103228

36. Martin GD, Hoath SD, Hutchings IM (2008) Inkjet printing - the physics of manipulating liquid jets and drops. J Phys Conf Ser 105:12001. https://doi.org/10.1088/1742-6596/105/1/012001

37. Schiaffino S, Sonin AA (1997) Molten droplet deposition and solidification at low Weber numbers. Phys Fluids 9:3172–3187. https://doi.org/10.1063/1.869434

38. Yarin AL (2006) Drop impact dynamics: splashing, spreading, receding, bouncing…. Annu Rev Fluid Mech 38:159–192. https://doi.org/10.1146/annurev.fluid.38.050304.092144

39. Jung S, Hwang HJ, Hong SH (2016) Drops on substrates. In: Hoath SD (ed) Fundamentals of inkjet printing: The science of inkjet and droplets. Wiley-VCH, Weinheim, pp 199–218

40. Zisman WA (1964) Relation of the equilibrium contact angle to liquid and solid constitution. In: Fowkes FM (ed) Advances in Chemistry, Vol. 43. American Chemical Society, Washington DC, pp 1–51

41. Fowkes FM (1964) Attractive forces at interfaces. Ind Eng Chem 56:40–52. https://doi.org/10.1021/ie50660a008

42. Wu S (2007) Calculation of interfacial tension in polymer systems. J Polym Sci Part C Polym Symp 34:19–30. https://doi.org/10.1002/polc.5070340105

43. Owens DK, Wendt RC (1969) Estimation of the surface free energy of polymers. J Appl Polym Sci 13:1741–1747. https://doi.org/10.1002/app.1969.070130815

44. Rabel W (1971) Einige Aspekte der Benetzungstheorie und ihre Anwendung auf die Untersuchung und Veränderung der Ober-flächeneigenschaften von Polymeren. Farbe und Lack 77:997–1005

45. Kaelble DH (1970) Dispersion-polar surface tension properties of organic solids. J Adhes 2:66–81. https://doi.org/10.1080/0021846708544582

46. Van Oss CJ, Chaudhury MK, Good RJ (1988) Interfacial Lifshitz-van der Waals and polar interactions in macroscopic systems. Chem Rev 88:927–941. https://doi.org/10.1021/cr00088a006

47. Li D, Neumann AW (1992) Equation of state for interfacial tensions of solid-liquid systems. Adv Colloid Interface Sci 39:299–345. https://doi.org/10.1016/0001-8686(92)80064-5

48. Marmur A, Valal D (2010) Correlating interfacial tensions with surface tensions: a Gibbsian approach. Langmuir 26:5568–5575. https://doi.org/10.1021/la9038478

49. Matavž A, Bobnar V, Malic B (2017) Tailoring ink-substrate interactions via thin polymeric layers for high-resolution printing. Langmuir 33(43):11893–11900. https://doi.org/10.1021/acs.langmuir.7b02181

50. Ramé E (1997) The interpretation of dynamic contact angles measured by the Wilhelmy Plate Method. J Colloid Interface Sci 185:245–251. https://doi.org/10.1006/jcis.1996.4589

51. Pierce E, Carmona FJ, Amirfazli A (2008) Understanding of sliding and contact angle results in tilted plate experiments. Colloids Surf A Physicochem Eng Asp 323:73–82. https://doi.org/10.1016/j.colsurfa.2007.09.032

52. Krishnan A, Liu Y-H, Cha P et al. (2005) An evaluation of methods for contact angle measurement. Colloids Surf B Biointerfaces 43:95–98. https://doi.org/10.1016/j.colsurfb.2005.04.003

53. De Gennes PG (1985) Wetting: Statics and dynamics. Rev Mod Phys 57:827–863. https://doi.org/10.1103/RevModPhys.57.827

54. Tadmor R (2004) Line energy and the relation between advancing, receding, and young contact angles. Langmuir 20:7659–7664. https://doi.org/10.1021/la049410h

55. Tadmor R (2013) Misconceptions in wetting phenomena. Langmuir 29:15474–15475. https://doi.org/10.1021/la403578q

56. Rodríguez-Valverde MA, Montes Ruiz-Cabello FJ, Gea Jódar PM et al. (2010) A new model to estimate the Young contact angle from contact angle hysteresis measurements. Colloids Surf

A Physicochem Eng Asp 365:21–27. https://doi.org/10.1016/j.colsurfa.2010.01.055

57. Marmur A (2006) Soft contact: measurement and interpretation of contact angles. Soft Matter 2:12–17. https://doi.org/10.1039/B514811C

58. Giacomello A, Schimmele L, Dietrich S (2016) Wetting hysteresis induced by nanodefects. Proc Natl Acad Sci 113:262–271. https://doi.org/10.1073/pnas.1513942113

59. Diddens C, Kuerten JGM, van der Geld CWM, Wijshoff HMA (2017) Modeling the evaporation of sessile multi-component droplets. J Colloid Interface Sci 487:426–436. https://doi.org/10.1016/j.jcis.2016.10.030

60. Oh JH, Lim SY (2010) Precise size control of inkjet-printed droplets on a flexible polymer substrate using plasma surface treatment. J Micromech Microeng 20:15030. https://doi.org/10.1088/0960-1317/20/1/015030

61. Jang J, Kang H, Chakravarthula HCN, Subramanian V (2015) Fully inkjet-printed transparent oxide thin film transistors using a fugitive wettability switch. Adv Electron Mater 1:1500086. https://doi.org/10.1002/aelm.201500086

62. Sakai Y, Futakuchi T, Iijima T, Adachi M (2006) Preparation of (Ba,Sr)TiO$_3$ thick film on ZrO$_2$ substrates by Inkjet printing. Jpn J Appl Phys, Part 1 Regul Pap Short Notes Rev Pap 45:846–849. https://doi.org/10.1143/JJAP.45.846

63. Wilbur JL, Kumar A, Biebuyck HA et al. (1996) Microcontact printing of self-assembled monolayers: applications in microfabrication. Nanotechnology 7:452–457. https://doi.org/10.1088/0957-4484/7/4/028

64. Nguyen PQM, Yeo LP, Lok BK, Lam YC (2014) Patterned surface with controllable wettability for inkjet printing of flexible printed electronics. ACS Appl Mater Interfaces 6:4011–4016. https://doi.org/10.1021/am4054546

65. Wang JZ, Zheng ZH, Li HW et al. (2004) Dewetting of conducting polymer inkjet droplets on patterned surfaces. Nat Mater 3:171–176. https://doi.org/10.1038/nmat1073

66. Janssen D, De Palma R, Verlaak S et al. (2006) Static solvent contact angle measurements, surface free energy and wettability determination of various self-assembled monolayers on silicon dioxide. Thin Solid Films 515:1433–1438. https://doi.org/10.1016/j.tsf.2006.04.006

67. Sele CW, von Werne T, Friend RH, Sirringhaus H (2005) Lithography-free, self-aligned inkjet printing with sub-hundred-nanometer resolution. Adv Mater 17:997–1001. https://doi.org/10.1002/adma.200401285

68. Davis SH (1980) Moving contact lines and rivulet instabilities. Part 1. Static rivulet J Fluid Mech 98:225. https://doi.org/10.1017/S0022112080000110

69. Schiaffino S, Sonin A (1997) Formation and stability of liquid and molten beads on a solid surface. J Fluid Mech 343:95–110. https://doi.org/10.1017/S0022112097005831

70. Soltman D, Subramanian V (2008) Inkjet-printed line morphologies and temperature control of the coffee ring effect. Langmuir 24:2224–2231. https://doi.org/10.1021/la7026847

71. Stringer J, Derby B (2009) Limits to feature size and resolution in ink jet printing. J Eur Ceram Soc 29:913–918. https://doi.org/10.1016/j.jeurceramsoc.2008.07.016

72. Hsiao W-K, Martin GD, Hutchings IM (2014) Printing Stable Liquid Tracks on a Surface with Finite Receding Contact Angle. Langmuir 30:12447–12455. https://doi.org/10.1021/la502490p

73. Kang H, Soltman D, Subramanian V (2010) Hydrostatic optimization of inkjet-printed films. Langmuir 26:11568–11573. https://doi.org/10.1021/la100822s

74. Soltman D, Smith B, Morris SJS, Subramanian V (2013) Inkjet printing of precisely defined features using contact-angle hysteresis. J Colloid Interface Sci 400:135–139. https://doi.org/10.1016/j.jcis.2013.03.006

75. Deegan R, Bakajin O, Dupont T et al. (2000) Contact line deposits in an evaporating drop. Phys Rev E Stat Phys Plasmas Fluids Relat Interdiscip Top 62:756–765

76. Ko H-Y, Park J, Shin H, Moon J (2004) Rapid self-assembly of monodisperse colloidal spheres in an ink-jet printed droplet. Chem Mater 16:4212–4215. https://doi.org/10.1021/cm035256t

77. Deegan R (2000) Pattern formation in drying drops. Phys Rev E Stat Phys Plasmas Fluids Relat Interdiscip Top 61:475–485

78. Harris DJ, Hu H, Conrad JC, Lewis JA (2007) Patterning colloidal films via evaporative lithography. Phys Rev Lett 98:148301. https://doi.org/10.1103/PhysRevLett.98.148301

79. van den Berg AMJ, de Laat AWM, Smith PJ et al. (2007) Geometric control of inkjet printed features using a gelating polymer. J Mater Chem 17:677. https://doi.org/10.1039/b612158f

80. Talbot EL, Yang L, Berson A, Bain CD (2014) Control of the particle distribution in inkjet printing through an evaporation-driven sol-gel transition. ACS Appl Mater Interfaces 6:9572–9583. https://doi.org/10.1021/am501966n

81. Hu H, Larson RG (2006) Marangoni effect reverses coffee-ring depositions. J Phys Chem B 110:7090–7094. https://doi.org/10.1021/jp0609232

82. Still T, Yunker PJ, Yodh AG (2012) Surfactant-induced Marangoni Eddies alter the coffee-rings of evaporating colloidal drops. Langmuir 28:4984–4988. https://doi.org/10.1021/la204928m

83. Kajiya T, Kobayashi W, Okuzono T, Doi M (2009) Controlling the drying and film formation processes of polymer solution droplets with addition of small amount of surfactants. J Phys Chem B 113:15460–15466. https://doi.org/10.1021/jp9077757

84. Park J, Moon J (2006) Control of colloidal particle deposit patterns within Picoliter droplets ejected by ink-jet printing. Langmuir 22:3506–3513. https://doi.org/10.1021/la053450j

85. Kim D, Jeong S, Park BK, Moon J (2006) Direct writing of silver conductive patterns: improvement of film morphology and conductance by controlling solvent compositions. Appl Phys Lett 89:264101. https://doi.org/10.1063/1.2424671

86. Babatunde PO, Hong WJ, Nakaso K, Fukai J (2013) Effect of solute- and solvent-derived Marangoni flows on the shape of polymer films formed from drying droplets. AIChE J 59:699–702. https://doi.org/10.1002/aic.14031

87. Poulard C, Damman P (2007) Control of spreading and drying of a polymer solution from Marangoni flows. Europhys Lett 80:64001. https://doi.org/10.1209/0295-5075/80/64001

88. Bathurst SP, Kim SG (2013) Printing of uniform PZT thin films for MEMS applications. CIRP Ann - Manuf Technol 62:227–230. https://doi.org/10.1016/j.cirp.2013.03.113

89. Kajiya T, Kaneko D, Doi M (2008) Dynamical visualization of "coffee stain phenomenon" in droplets of polymer solution via fluorescent microscopy. Langmuir 24:12369–12374. https://doi.org/10.1021/la8017858

90. Fukai J, Ishizuka H, Sakai Y et al. (2006) Effects of droplet size and solute concentration on drying process of polymer solution droplets deposited on homogeneous surfaces. Int J Heat Mass Transf 49:3561–3567. https://doi.org/10.1016/j.ijheatmasstransfer.2006.02.049

91. Li Y, Lan L, Sun S et al. (2017) All inkjet-printed metal-oxide thin-film transistor array with good stability and uniformity using surface-energy patterns. ACS Appl Mater Interfaces 9:8194–8200. https://doi.org/10.1021/acsami.7b00435

92. Kim D, Jeong Y, Song K et al. (2009) Inkjet-printed zinc tin oxide thin-film transistor. Langmuir 25:11149–11154. https://doi.org/10.1021/la901436p

93. Robin M, Kuai W, Amela-Cortes M et al. (2015) Epoxy based ink as versatile material for inkjet-printed devices. ACS Appl Mater Interfaces 7:21975–21984. https://doi.org/10.1021/acsami.5b06678

94. Kajiya T, Monteux C, Narita T et al. (2009) Contact-line recession leaving a macroscopic polymer film in the drying droplets of water–poly(N, N -dimethylacrylamide) (PDMA) solution. Langmuir 25:6934–6939. https://doi.org/10.1021/la900216k

95. Fukuda K, Sekine T, Kumaki D, Tokito S (2013) Profile control of inkjet printed silver electrodes and their application to organic transistors. ACS Appl Mater Interfaces 5:3916–3920. https://doi.org/10.1021/am400632s

96. Parsa M, Harmand S, Sefiane K et al. (2015) Effect of substrate temperature on pattern formation of nanoparticles from volatile drops. Langmuir 31:3354–3367. https://doi.org/10.1021/acs.langmuir.5b00362

97. Tao R, Ning H, Fang Z et al. (2017) Homogeneous surface profiles of inkjet-printed silver nanoparticle films by regulating their drying microenvironment. J Phys Chem C 121:8992–8998. https://doi.org/10.1021/acs.jpcc.6b12793

98. Hu S, Wang Y, Man X, Doi M (2017) Deposition patterns of two neighboring droplets: onsager variational principle studies. Langmuir 33:5965–5972. https://doi.org/10.1021/acs.langmuir.7b01354

99. Kobayashi M, Makino M, Okuzono T, Doi M (2010) Interference effects in the drying of polymer droplets on substrate. J Phys Soc Jpn 79:44802. https://doi.org/10.1143/JPSJ.79.044802

100. Diddens C, Tan H, Lv P et al. (2017) Evaporating pure, binary and ternary droplets: thermal effects and axial symmetry breaking. J Fluid Mech 823:470–497. https://doi.org/10.1017/jfm.2017.312

101. Sáenz PJ, Wray AW, Che Z et al. (2017) Dynamics and universal scaling law in geometrically-controlled sessile drop evaporation. Nat Commun 8:14783. https://doi.org/10.1038/ncomms14783

102. Zeumault A, Ma S, Holbery J (2016) Fully inkjet-printed metal-oxide thin-film transistors on plastic. Phys Status Solidi 213:2189–2195. https://doi.org/10.1002/pssa.201600077

103. Frunză RC, Kmet B, Jankovec M et al. (2014) Ta_2O_5-based high-K dielectric thin films from solution processed at low temperatures. Mater Res Bull 50:323–328. https://doi.org/10.1016/j.materresbull.2013.11.025

104. Vescio G, López-Vidrier J, Leghrib R et al. (2016) Flexible inkjet printed high-k HfO_2 -based MIM capacitors. J Mater Chem C 4:1804–1812. https://doi.org/10.1039/C5TC03307A

105. Tellier J, Kuščer D, Malič B et al. (2010) Transparent, amorphous and organics-free ZnO thin films produced by chemical solution deposition at 150 °C. Thin Solid Films 518:5134–5139. https://doi.org/10.1016/j.tsf.2010.03.010

106. Lee JS, Kwack Y-J, Choi W-S (2013) Inkjet-printed In_2O_3 thin-film transistor below 200 °C. ACS Appl Mater Interfaces 5:11578–11583. https://doi.org/10.1021/am4025774

107. Scheideler WJ, Kumar R, Zeumault AR, Subramanian V (2017) Low-temperature-processed printed metal oxide transistors based on pure aqueous inks. Adv Funct Mater 27:1606062. https://doi.org/10.1002/adfm.201606062

108. Leppäniemi J, Eiroma K, Majumdar H, Alastalo A (2017) Far-UV annealed inkjet-printed In_2O_3 semiconductor layers for thin-film transistors on a flexible polyethylene naphthalate substrate. ACS Appl Mater Interfaces 9:8774–8782. https://doi.org/10.1021/acsami.6b14654

109. Hoffmann RC, Dilfer S, Schneider JJ (2011) Transparent indium tin oxide as inkjet-printed thin film electrodes for organic field-effect transistors. Phys Status Solidi 208:2920–2925. https://doi.org/10.1002/pssa.201127362

110. Song K, Jung Y, Kim Y et al. (2011) Solution-processable tin-doped indium oxide with a versatile patternability for transparent oxide thin film transistors. J Mater Chem 21:14646. https://doi.org/10.1039/c1jm11418b

111. Fang M, Aristov A, Rao KV et al. (2013) Particle-free inkjet printing of nanostructured porous indium tin oxide thin films. RSC Adv 3:19501. https://doi.org/10.1039/c3ra40487k

112. Hennek JW, Xia Y, Everaerts K et al. (2012) Reduced contact resistance in inkjet printed high-performance amorphous indium gallium zinc oxide transistors. ACS Appl Mater Interfaces 4:1614–1619. https://doi.org/10.1021/am201776p

113. Kim GH, Kim HS, Shin HS et al. (2009) Inkjet-printed InGaZnO thin film transistor. Thin Solid Films 517:4007–4010. https://doi.org/10.1016/j.tsf.2009.01.151

114. Avis C, Hwang HR, Jang J (2014) Effect of channel layer thickness on the performance of indium–zinc–tin oxide thin film transistors manufactured by inkjet printing. ACS Appl Mater Interfaces 6:10941–10945. https://doi.org/10.1021/am501153w

115. Lee D-H, Han S-Y, Herman GS, Chang C (2009) Inkjet printed high-mobility indium zinc tin oxide thin film transistors. J Mater Chem 19:3135. https://doi.org/10.1039/b822893k

116. Avis C, Jang J (2011) A high performance inkjet printed zinc tin oxide transparent thin-film transistor manufactured at the maximum process temperature of 300 °C and its stability test. Electrochem Solid-State Lett 14:9–11. https://doi.org/10.1149/1.3516608

117. Vernieuwe K, Cuypers D, Kirschhock CEA et al. (2017) Thermal processing of aqueous AZO inks towards functional TCO thin films. J Alloy Compd 690:360–368. https://doi.org/10.1016/j.jallcom.2016.08.120

118. Matavž A, Frunza RC, Drnovsek A et al. (2016) Inkjet printing of thin metal-oxide structures from sol-gel precursor inks. In: 2016 Joint IEEE International Symposium on the Applications of Ferroelectrics, European Conference on Application of Polar Dielectrics, and Piezoelectric Force Microscopy Workshop (ISAF/ECAPD/PFM). IEEE, pp 1–4

119. Morozova M, Kluson P, Krysa J et al. (2011) Thin TiO_2 films prepared by inkjet printing of the reverse micelles sol–gel composition. Sens Actuators B Chem 160:371–378. https://doi.org/10.1016/j.snb.2011.07.063

120. Chouiki M, Schoeftner R (2011) Inkjet printing of inorganic sol-gel ink and control of the geometrical characteristics. J Sol-Gel Sci Technol 58:91–95. https://doi.org/10.1007/s10971-010-2360-0

121. Machida O, Shimofuku A, Tashiro R et al. (2012) Fabrication of lead zirconate titanate films by inkjet printing. Jpn J Appl Phys 51. https://doi.org/10.1143/JJAP.51.09LA11

122. Bathurst SP (2012) Ink Jet Printing of PZT Thin Films for MEMS. PhD thesis, Massachusetts Institute of Technology

123. Kaydanova T, Miedaner A, Perkins JD et al. (2007) Direct-write inkjet printing for fabrication of barium strontium titanate-based tunable circuits. Thin Solid Films 515:3820–3824. https://doi.org/10.1016/j.tsf.2006.10.009

124. Pečnik T, Glinšek S, Kmet B, Malič B (2015) Combined effects of thickness, grain size and residual stress on the dielectric properties of $Ba_{0.5}Sr_{0.5}TiO_3$ thin films. J Alloy Compd 646:766–772. https://doi.org/10.1016/j.jallcom.2015.06.192

125. List FA, Kodenkandath T, Rupich MW (2007) Fabrication of filamentary YBCO coated conductor by inkjet printing. IEEE Trans Appl Supercond 17:3355–3358. https://doi.org/10.1109/TASC.2007.899991

126. Feys J, Vermeir P, Lommens P et al. (2012) Ink-jet printing of $YBa_2Cu_3O_7$ superconducting coatings and patterns from aqueous solutions. J Mater Chem 22:3717–3726. https://doi.org/10.1039/C1JM14899K

127. Gadea C, Hanniet Q, Lesch A et al. (2017) Aqueous metal–organic solutions for YSZ thin film inkjet deposition. J Mater Chem C 5:6021–6029. https://doi.org/10.1039/C7TC01879G

128. Bacelis-Martínez RD, Oskam G, Rodriguez Gattorno G, Ruiz-Gómez MA (2017) Inkjet printing as high-throughput technique for the fabrication of $NiCo_2O_4$ films. Adv Mater Sci Eng 2017:1–9. https://doi.org/10.1155/2017/9647458

129. Wang C, Tomov RI, Vasant Kumar R, Glowacki BA (2011) Inkjet printing of gadolinium-doped ceria electrolyte on NiO-YSZ substrates for solid oxide fuel cell applications. J Mater Sci 46:6889–6896. https://doi.org/10.1007/s10853-011-5653-y

130. Mosiadz M, Tomov RI, Hopkins SC et al. (2010) Inkjet printing of $Ce_{0.8}Gd_{0.2}O_2$ thin films on Ni-5%W flexible substrates. J Sol-Gel Sci Technol 54:154–164. https://doi.org/10.1007/s10971-010-2170-4

131. Singh A, Gupta SK, Garg A (2017) Inkjet printing of NiO films and integration as hole transporting layers in polymer solar cells. Sci Rep 7:1775. https://doi.org/10.1038/s41598-017-01897-9

132. Brisse R, Faddoul R, Bourgeteau T et al. (2017) Inkjet printing NiO-based p-type dye-sensitized solar cells. ACS Appl Mater Interfaces 9:2369–2377. https://doi.org/10.1021/acsami.6b12912

133. Cheng Z, Xing R, Hou Z et al. (2010) Patterning of light-emitting YVO_4:Eu^{3+} thin films via inkjet printing. J Phys Chem C 114:9883–9888. https://doi.org/10.1021/jp101941y

134. Lee D, Wang W, Gutu T et al. (2008) Biogenic silica based Zn_2SiO_4:Mn^{2+} and Y_2SiO_5:Eu^{3+} phosphor layers patterned by inkjet printing process. J Mater Chem 18:3633. https://doi.org/10.1039/b806812g

135. Jiang J, Bao B, Li M et al. (2016) Fabrication of transparent multilayer circuits by inkjet printing. Adv Mater 28:1420–1426. https://doi.org/10.1002/adma.201503682

136. Clemens S, Schneller T (2013) Template Controlled Growth. In: Schneller T, Waser R, Kosec M, Payne D (eds) Chemical Solution Deposition of Functional Oxide Thin Films. Springer Vienna, Vienna, pp 517–539

137. Bormashenko E, Eldar B, Chaniel G et al. (2016) Influence of cold radiofrequency air and nitrogen plasmas treatment on wetting of polypropylene by the liquid epoxy resin. Colloids Surf A Physicochem Eng Asp 506:445–449. https://doi.org/10.1016/j.colsurfa.2016.07.028

138. Jiang C, Zhong Z, Liu B et al. (2016) Coffee-ring-free quantum dot thin film using inkjet printing from a mixed-solvent system on modified ZnO transport layer for light-emitting devices. ACS Appl Mater Interfaces 8:26162–26168. https://doi.org/10.1021/acsami.6b08679

139. Lide DR (2004) CRC handbook of chemistry and physics, 84th edn. CRC Press, Boca Raton